

NIHAO XVII: The diversity of dwarf galaxy kinematics and implications for the HI velocity function

Aaron A. Dutton^{1*}, Aura Obreja^{1,2}, Andrea V. Macciò^{1,3}

¹*New York University Abu Dhabi, PO Box 129188, Saadiyat Island, Abu Dhabi, United Arab Emirates*

²*University Observatory Munich, Scheinerstraße 1, D-81679 Munich, Germany*

³*Max Planck Institute für Astronomie, Königstuhl 17, 69117 Heidelberg, Germany*

15 November 2018

ABSTRACT

We use 85 pairs of high resolution LCDM cosmological simulations from the NIHAO project to investigate why in dwarf galaxies neutral hydrogen (HI) linewidths measured at 50% of the peak flux $W_{50}/2$ (from the hydrodynamical simulations) tend to under-predict the maximum circular velocity V_{\max}^{DMO} (from the corresponding dark matter only simulations). There are two main contributing processes. 1) Lower mass galaxies are less rotationally supported. This is confirmed observationally from the skewness of linewidths in bins of HI mass in both ALFALFA and HIPASS observations. 2) The HI distributions are less extended (relative to the dark matter halo) in dwarf galaxies. Coupled to the lower baryon-to-halo ratio results in rotation curves that are still rising at the last measured data point, in agreement with observations from SPARC. Combining these two effects, in both simulations and observations lower mass galaxies have, on average, lower W_{50}/W_{20} . Additionally, mass loss driven by supernovae and projection effects (dwarf galaxies are in general not thin disks) further reduce the linewidths. The implied HI linewidth velocity function from NIHAO is in good agreement with observations in the nearby Universe of dwarf galaxies: $10 < W_{50}/2 < 80 \text{ km s}^{-1}$. The dark matter only slope of ≈ -2.9 is reduced to ≈ -1.0 in the hydro simulations. Future radio observations of unbiased samples with higher spatial resolution will enable stricter tests of the simulations, and thus of the LCDM model.

Key words: cosmology: theory – dark matter – galaxies: formation – galaxies: kinematics and dynamics – galaxies: structure – methods: numerical

1 INTRODUCTION

The Lambda Cold Dark Matter (LCDM) model is very successful in reproducing the large scale structure of the Universe (Springel et al. 2005) and the anisotropies in the Cosmic Microwave Background (Planck Collaboration et al. 2014). In a LCDM universe there is a larger number of low mass structures compared to more massive ones, or in other words a steeply declining halo mass function $N(M) \propto M^{-1}$ or halo velocity function $N(V) \propto V^{-3}$ (Klypin et al. 2015). This prediction is naively at odds with observational data around galaxies, i.e. the satellite abundance (Klypin et al. 1999; Moore et al. 1999). This “missing satellite” problem has natural baryonic solution: galaxy formation becomes increasingly inefficient in low-mass dark matter haloes, due to the ionizing background, supernovae (SN) explosions and gas removal due to ram pres-

sure (Bullock et al. 2000; Benson et al. 2002; Kravtsov et al. 2004; Macciò et al. 2010). The latest cosmological hydrodynamical simulations of the Local Group are now consistent with the observed satellite stellar mass and velocity functions (e.g., Sawala et al. 2016; Buck et al. 2018).

The velocity function of galaxies using HI linewidths has been measured in the nearby universe (within ~ 200 Mpc) from the HIPASS (Zwaan et al. 2010) and ALFALFA surveys (Papastergis et al. 2011), and within the Local Volume (within 10 Mpc) by Klypin et al. (2015). These and other authors (Zavala et al. 2009; Trujillo-Gomez et al. 2011) have shown that LCDM provides very good estimates of the number of galaxies with circular velocities around and above 80 km s^{-1} . With a careful treatment of various systematics including survey selection effects Obreschkow et al. (2013) showed agreement between LCDM down to circular velocities of $\sim 60 \text{ km s}^{-1}$. However, LCDM appears to fail quite dramatically at lower circular velocities, overestimating by a factor of $\simeq 3$ the number of dwarf galaxies at velocity

* dutton@nyu.edu

scale of 50 km s^{-1} , and by a factor of $\simeq 5$ at velocity scale of 30 km s^{-1} (Klypin et al. 2015). Galaxies at these velocity scales are essentially insensitive to the ionization background and, by not being satellites, they are not affected by gas depletion via ram pressure or by stellar stripping. This makes the mismatch between the observed linewidth function and the halo velocity function a more serious challenge to the LCDM paradigm. Furthermore, simple modifications to the LCDM paradigm, such as warm dark matter, are unable to resolve this issue as candidates with a warm enough particle to significantly reduce the number density of dark matter haloes result in a characteristic scale in the velocity function that is not observed (Klypin et al. 2015). The normalization of the velocity function is dependent on key cosmological parameters such as the amplitude of primordial perturbations (σ_8) and the total matter density (Ω_m) (Schneider & Trujillo-Gomez 2018). For example, the difference between a Planck (Planck Collaboration et al. 2014) and WMAP7 (Jarosik et al. 2011) cosmology is a factor of 1.43 in number density at fixed velocity (Klypin et al. 2015).

The solution to this discrepancy is that in dwarf galaxies HI linewidths measured at 50% of the peak flux, W_{50} , are a poor tracer of the maximum circular velocity of the host dark matter halo (Brook & Di Cintio 2015; Macciò et al. 2016; Brooks et al. 2017; Verbeke et al. 2017). This should not be a surprise, since it is generally known that lower mass and younger galaxies are less rotationally supported than higher mass, and older galaxies. This is seen in both observations (e.g. Kassin et al. 2012; Newman et al. 2013; Wisnioski et al. 2015), and hydrodynamical galaxy formation simulations (Ceverino et al. 2017; El-Badry et al. 2018). Furthermore, as discussed in Courteau (1997), unlike resolved HI rotation curves, HI linewidths do not necessarily sample outer disks effectively since the HI surface density drops rapidly beyond the optical radius.

In this paper we investigate the cause of the difference between $W_{50}/2$ and $V_{\text{max}}^{\text{DMO}}$ further using galaxy formation simulations from the NIHAO project (Wang et al. 2015). Possible explanations we consider include: gas mass loss from the halo – resulting in lower circular velocity in the hydro than dark matter only simulation; HI in the simulations is not extended enough – so that the maximum rotation velocity does not reach the maximum circular velocity; Non-circular motions – resulting in the rotation curve underestimating the circular velocity; Projection effects – due to dwarf galaxies not being thin rotating disks.

The outline of the paper is as follows. Section 2 describes the cosmological hydrodynamical simulations and the various velocity definitions we use. In Section 3 we present the transformation from maximum circular velocity to HI linewidth. In section 4 we present the implied HI velocity function from our simulations. In section 5 we discuss what causes the linewidths to underestimate the maximum halo velocity, and present observational tests of these effects. A summary is given in section 6.

2 SIMULATIONS

Here we give a brief overview of the NIHAO simulations. We refer the reader to Wang et al. (2015) for a more complete discussion. NIHAO is a sample of ~ 90 hydrodynam-

ical cosmological zoom-in simulations using the SPH code GASOLINE2 (Wadsley et al. 2017).

Halo selection is performed at redshift $z = 0$ from parent dissipationless simulations of size 60, 20, & 15 Mpc/h, presented in Dutton & Macciò (2014) which adopt a flat Λ CDM cosmology with parameters from the Planck Collaboration et al. (2014): Hubble parameter $H_0 = 67.1 \text{ km s}^{-1} \text{ Mpc}^{-1}$, matter density $\Omega_m = 0.3175$, dark energy density $\Omega_\Lambda = 1 - \Omega_m = 0.6825$, baryon density $\Omega_b = 0.0490$, power spectrum normalization $\sigma_8 = 0.8344$, power spectrum slope $n = 0.9624$. Halo selection is uniform in log halo mass from ~ 10 to ~ 12 *without* reference to the halo merger history, concentration or spin parameter. Star formation and feedback is implemented as described in Stinson et al. (2006, 2013). Mass and force softening are chosen to resolve the mass profile at $\lesssim 1\%$ the virial radius, which results in $\sim 10^6$ dark matter particles inside the virial radius of all haloes at $z = 0$. The motivation of this choice is to ensure that the simulations resolve the galaxy dynamics on the scale of the half-light radii, which are typically $\sim 1.5\%$ of the virial radius (Kravtsov 2013). Hydro particles have force softening a factor of 2.34 smaller than the dark matter particles, and range from $\simeq 75 \text{ pc}$ in the lowest mass haloes to $\simeq 400 \text{ pc}$ in the most massive haloes.

Each hydro simulation has a corresponding dark matter only (DMO) simulation of the same resolution. These simulations have been started using the identical initial conditions, replacing baryonic particles with dark matter particles. We remove the four most massive haloes (g1.12e12, g1.77e12, g1.92e12, g2.79e12), as these have formed too many stars, in particular near the galaxy centers, resulting in strongly peaked central circular velocity profiles (Wang et al. 2015). The final sample used in this work consists of 85 simulations.

Halo selection in NIHAO zoom-in simulations was identified using the MPI+OpenMP hybrid halo finder AHF¹ (Gill et al. 2004; Knollmann & Knebe 2009). AHF locates local overdensities in an adaptively smoothed density field as prospective halo centers. The virial masses of the haloes are defined as the masses within a sphere whose average density is 200 times the cosmic critical matter density, $\rho_{\text{crit}} = 3H_0^2/8\pi G$. The virial mass, size and circular velocity of the hydro simulations are denoted: $M_{200}, R_{200}, V_{200}$. The corresponding properties for the dark matter only simulations are denoted with a superscript, DMO. For the baryons we calculate masses enclosed within spheres of radius $r_{\text{gal}} = 0.2R_{200}$, which corresponds to ~ 10 to $\sim 50 \text{ kpc}$. The stellar mass inside r_{gal} is M_{star} , the neutral hydrogen, inside r_{gal} is computed following Rahmati et al. (2013) as described in Gutcke et al. (2017). In principle the neutral hydrogen should be separated further into atomic (HI), and molecular, (H_2), gas. In practice this has only marginal impact on the derived HI linewidths. This is expected because in dwarf galaxies the ratio between molecular and atomic gas is very low, while in high mass galaxies both atomic and molecular gas trace the same flat rotation velocity, albeit from gas at different radii. As a fiducial choice we consider atomic gas to be neutral gas with a density less than 10 cm^{-3} (which is also the star formation threshold used in our simulations).

¹ <http://popia.ft.uam.es/AMIGA>

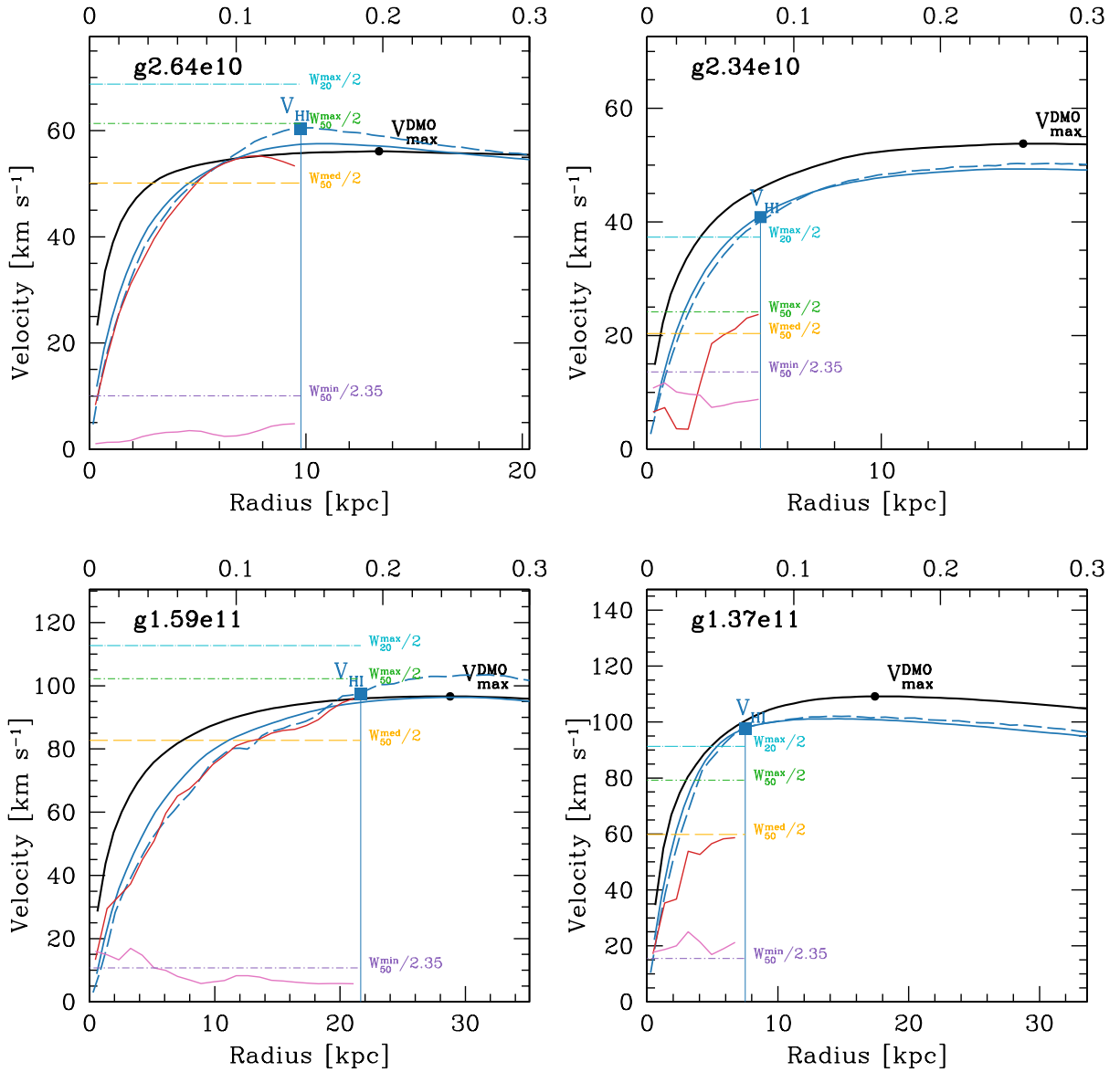


Figure 1. Example velocity profiles of four galaxies illustrating the different velocity definitions. The black line shows the spherical circular velocity of the dark matter only simulation. The black circle shows the maximum of this curve, V_{\max}^{DMO} , which typically occurs at $\approx 20\%$ of the virial radius, R_{200} , (upper axis). The two galaxies in the upper panels have $V_{\max}^{\text{DMO}} \sim 55 \text{ km s}^{-1}$, while the galaxies in the lower panels have $V_{\max}^{\text{DMO}} \sim 100 \text{ km s}^{-1}$. The blue lines show the circular velocity of the hydrodynamical simulation using the spherically enclosed mass (solid lines) and the potential in the disk plane (dashed). The left panels show galaxies where the rotation curve (red) traces the circular velocity from the potential (blue-dashed), and the maximum linewidth $W_{50}/2$ (green dashed line) equals the circular velocity at the HI radius, V_{HI} (blue square). The right panels show galaxies where the rotation curve underpredicts the circular velocity, and $W_{50}/2$ underestimates V_{HI} . The pink lines show the bulk velocity dispersion of the HI gas. A global measurement of the gas dispersion (including the thermal broadening) is given by the minimum HI linewidth / 2.35 (purple lines).

We measure galaxy velocities using a number of definitions as discussed below.

The NIHAO simulations are the largest set of cosmological zoom-ins covering the halo mass range 10^{10} to $10^{12} M_{\odot}$. Their uniqueness is in the combination of high spatial resolution coupled to a statistical sample of haloes. In the context of LCDM they form the “right” amount of stars both today and at earlier times (Wang et al. 2015). Their cold gas masses and sizes are consistent with observations (Stinson et al. 2015; Macciò et al. 2016), they follow the gas,

stellar, and baryonic Tully-Fisher relations (Dutton et al. 2017), and they reproduce the diversity of dwarf galaxy rotation curve shapes Santos-Santos et al. (2018). As such they provide a good template with which to connect galaxy observables (such as HI linewidths) to intrinsic properties of the host dark matter halo (such as maximum circular velocity).

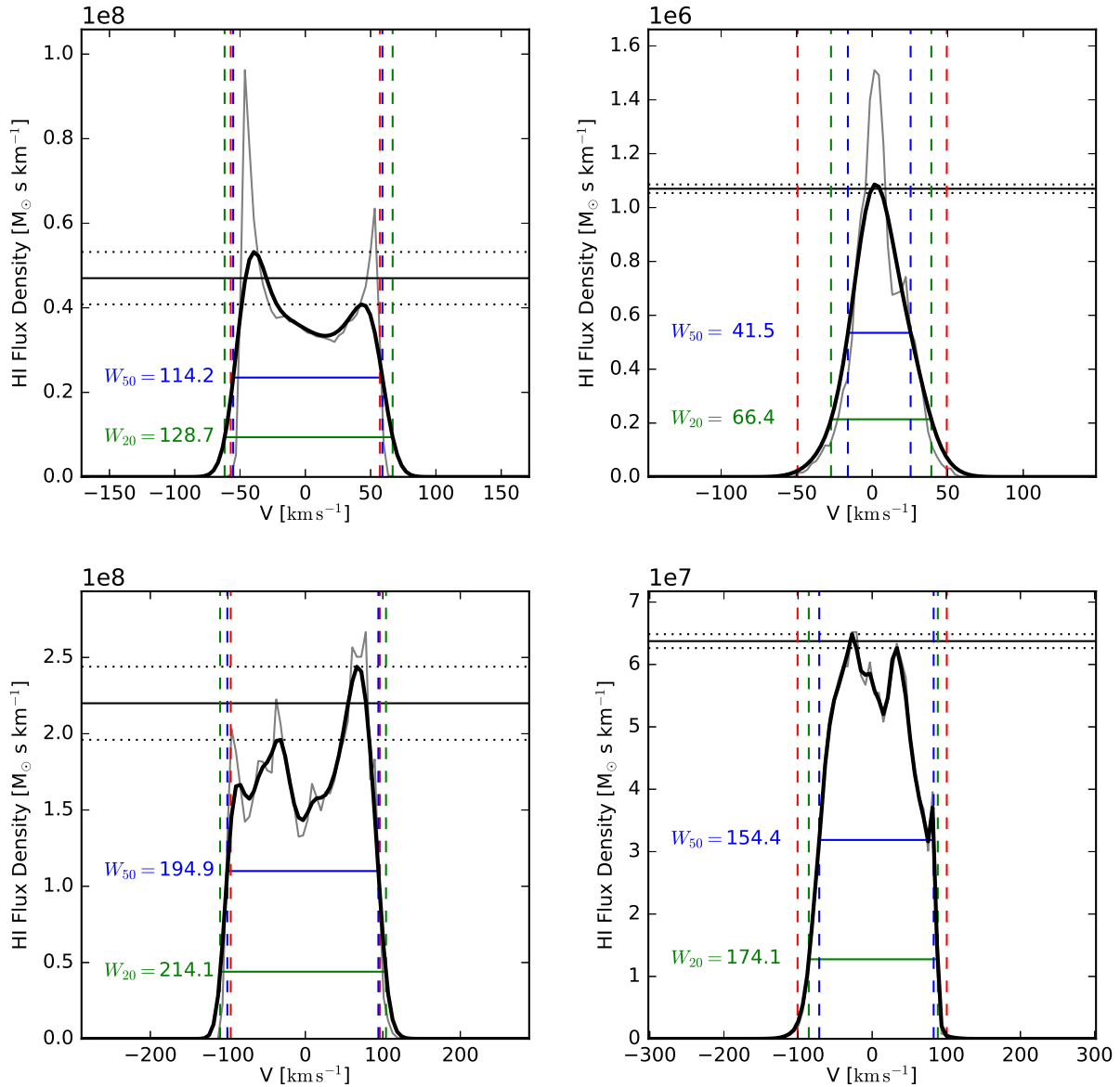


Figure 2. Example HI line profiles for edge-on projections of the four galaxies from Fig. 1 illustrating the different linewidth definitions. The black line shows the line profile including the thermal broadening, while the thin grey line shows the line profile from the kinematics only. The differences are only significant for the low velocity haloes. The horizontal dashed lines show the peak fluxes from either velocity side, while the horizontal solid line shows the average peak flux. The 50 and 20% peak fluxes are given with blue and green horizontal lines respectively. The vertical blue and green dashed lines show the corresponding velocities at the 50 and 20% peak fluxes. The red vertical line shows the maximum circular velocity of the dark matter halo, $V_{\text{max}}^{\text{DMO}}$.

2.1 Velocity definitions

We use a number of velocity definitions in this paper. We define them with the help of some examples as shown in Fig. 1. These galaxies were chosen to represent both rotationally supported galaxies (left panels) and those with more pressure support (right panels).

- $V_{\text{max}}^{\text{DMO}}$ – **maximum circular velocity of the DMO simulation.** We start with the spherical circular velocity profile of the dark matter only simulation (solid black line), which is equivalent to the cumulative mass profile $M(< r) = r V(r)^2 / G$. The maximum spherical circular ve-

locity is shown as a black circle, and occurs at 15% to 25% of the virial radius, R_{200} (upper axis scale).

- V_{max} – **maximum circular velocity of hydro simulation.** We next consider the circular velocity profile of the hydrodynamical simulation (blue lines). The solid line shows the spherical circular velocity, while the dashed line shows that derived from the potential in the disk plane, $V_{\text{pot}}^2 = -R\partial\Phi/\partial R$. We define $V_{\text{max}} \equiv V_{\text{circ}}(R_{\text{max}}^{\text{DMO}})$ as the spherical circular velocity of the hydro simulation at the radius where the maximum circular velocity of the DMO simulation occurs. We use this definition as it explicitly shows when there is mass loss from the system ($V_{\text{max}} < V_{\text{max}}^{\text{DMO}}$),

and where there is baryon dissipation ($V_{\max} > V_{\max}^{\text{DMO}}$). In these examples, there is mass loss from the galaxies in the right panels in Fig. 1, and no change for the galaxies in the left panels.

Notice that the potential based circular velocity is lower than the spherical circular velocity at small radii, and higher at large radii. This is a well known feature of the differences between a flattened and spherical mass distribution (Binney & Tremaine 1987)

- **V_{HI} - circular velocity at HI radius.** We define the HI radius, R_{HI} , as enclosing 90% of the HI mass (in the face-on projection). This approximates the edge of the observable HI rotation curve, and occurs close to the radius where the projected HI surface density profile reaches $1\text{M}_{\odot}\text{pc}^{-2}$, but it has the advantage of being free from projection effects and is measurable in every galaxy (that contains HI). The potential based circular velocity at the HI radius is then, $V_{\text{HI}} \equiv V_{\text{circ}}(R_{\text{HI}})$.

- **$V_{\text{rot}}(R), \sigma(R)$ – rotation and dispersion profile.** We calculate the rotation curve (red line), and dispersion profile (pink line) as follows. We rotate the galaxy to a face-on view, using the angular momentum of the cold ($T < 15000\text{K}$) gas particles inside 10% of the virial radius. We then divide the galaxy into a series of annuli of equal width. In each ring we calculate the mean velocity (V_{rot}) and velocity dispersion (σ) in the azimuthal (ϕ) direction. Note that this dispersion only takes into account the bulk motions of the gas. In the galaxies in the left panels, the rotation velocity closely traces the potential based circular velocity, and the dispersion is low, $\sim 5 - 10\text{km s}^{-1}$. In the galaxies in the right panels, the rotation velocity systematically under-predicts the circular velocity, and the velocity dispersion is higher, $\sim 10 - 20\text{km s}^{-1}$.

- **W_{50}, W_{20} - HI linewidths.** We next consider the HI linewidths, measured at 50% and 20% of the peak flux (see Fig. 2 for examples from our reference galaxies). In an update to the calculation in Macciò et al. (2016) here we include the thermal motions of the HI gas. At large linewidths the changes are minor, but for small linewidths the temperature adds a floor to the linewidth of $\sim 20\text{km s}^{-1}$, corresponding to $\sigma \sim 8.5\text{km s}^{-1}$. For each gas particle we represent the line-of-sight velocity distribution with a Gaussian with mean corresponding to the line-of-sight velocity of the particle, a flux corresponding to the HI mass of the particle, and a dispersion computed from the temperature of the particle assuming $\sigma = \sqrt{k_{\text{B}}T/m_{\text{H}}} = 9.09[\text{km s}^{-1}]\sqrt{T/10000\text{K}}$. We sum up the Gaussians to give the flux vs velocity histogram.

As is commonly done in observations, we define the peak flux as the average of the peak flux on each velocity wing (i.e., positive and negative). See Fig. 2 for examples. The peak fluxes on each velocity wing are marked with dotted horizontal lines. The average of these is shown with solid horizontal lines. By definition $W_{20} \geq W_{50}$. Because W_{20} requires higher signal to noise, and thus can be measured from fewer galaxies, W_{50} is the more commonly used definition in large HI surveys, so will be our default definition.

We calculate the linewidths from 100 random projections (uniformly selected from the surface of a unit sphere), and measure the maximum, median, and minimum values. The maximum values typically correspond to the values derived from an edge-on view of the galaxy. They are shown as cyan

(W_{20}^{\max}) and green (W_{50}^{\max}) horizontal lines in Fig. 1. The median $W_{50}/2$ is shown with an orange horizontal line. The minimum linewidth (purple horizontal lines) can be used to approximate the gas velocity dispersion of the system, since for a Gaussian, $\sigma = W_{50}/2.35$.

For each projection where we measure a linewidth we also measure the minor to major axis ratio (b/a) of the HI gas using moments as follows. For each gas particle we have its projected coordinates, (x, y) , distance from the galaxy center $R^2 = x^2 + y^2$, and HI mass, m . Using these quantities we calculate the moments weighted by the HI mass:

$$Sxx = \left(\sum mx^2/R^2 \right) / \sum m, \quad (1)$$

$$Syy = \left(\sum my^2/R^2 \right) / \sum m, \quad (2)$$

$$Sxy = \left(\sum mxy/R^2 \right) / \sum m. \quad (3)$$

The axis ratio is then given by

$$(b/a) = \frac{1 - \sqrt{Q^2 + U^2}}{1 + \sqrt{Q^2 + U^2}}, \quad (4)$$

where $Q = Sxx - Syy$ and $U = 2Sxy$.

3 FROM MAXIMUM CIRCULAR VELOCITY TO HI LINEWIDTH

Fig. 3 shows the relations between half-linewidths $W_{50}/2$ and $W_{20}/2$ with V_{\max}^{DMO} . The left panel is very similar to Fig.2 of Macciò et al. (2016), but here we use an updated calculation of the linewidth which introduces a floor to the linewidth of $W_{50} \sim 20\text{km s}^{-1}$. Galaxies lie systematically below the one-to-one relation (dotted lines) indicating the HI linewidth is a biased tracer of the maximum halo velocity. Linear fits to the relations (using all the data points) are given by

$$\log(W_{50}/2) = 1.614 + 1.557(\log V_{\max}^{\text{DMO}} - 1.904), \quad (5)$$

with a scatter of $\sigma = 0.16$, and

$$\log(W_{20}/2) = 1.751 + 1.419(\log V_{\max}^{\text{DMO}} - 1.904), \quad (6)$$

with a scatter of $\sigma = 0.12$. The slope of these fits is greater than unity, showing that linewidths are a poorer tracer of halo velocity in lower velocity haloes. The scatters show that W_{50} is a poorer tracer of the halo velocity than W_{20} .

Fig. 4 shows the relations between various velocity definitions and V_{\max}^{DMO} . Linear fits (in log – log space) are given in Table. 1. Notice that the normalization, slope, and scatter systematically change at each step. At anyone of these steps the changes are not large, but they accumulate to a relation between linewidth and halo velocity that is very different from a one-to-one correspondence. For galaxies in Milky Way mass haloes $V_{\max}^{\text{DMO}} \simeq 180\text{km s}^{-1}$ the average projected half-linewidth is $W_{50}/2 = 141\text{km s}^{-1}$, so that up to the expected project effects, the linewidth is a good tracer of the maximum halo velocity. However, for dwarf galaxies at $V_{\max}^{\text{DMO}} \simeq 50\text{km s}^{-1}$ the average half-linewidth of $W_{50}^{\text{med}}/2 \simeq 20\text{km s}^{-1}$, is a factor of 2.5 times lower than the halo velocity.

There are a number of physical processes that play a role in the conversion of maximum circular velocity into projected HI linewidths: inflows and outflows; HI extent and

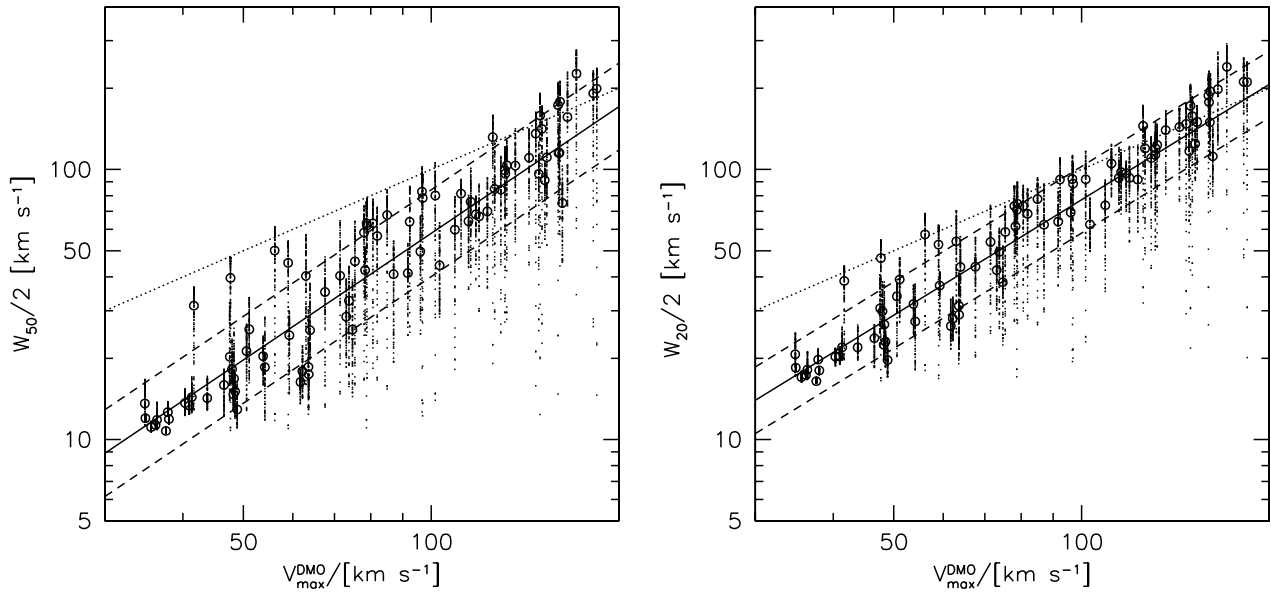


Figure 3. Relation between HI linewidths, W_{50} (left), and W_{20} (right) from the hydro simulations and maximum circular velocity from the corresponding dark matter only simulations. The points show 100 random projections per galaxy, with the open circle showing the median linewidth. The dotted line shows the one-to-one relation. The solid line shows a fit to all the data, with the 1σ scatter shown with dashed lines.

Table 1. Linear fits of the form $y = a + b(x - x_0)$ to various scaling relations. For all relations x_0 is chosen to equal the mean of x . The scatter of the data about the model is σ_y .

Sample	y	x	x_0	a	b	σ_y	Fig.
NIHAO	$\log_{10}(W_{50}/2[\text{km s}^{-1}])$	$\log_{10}(V_{\text{max}}^{\text{DMO}}/[\text{km s}^{-1}])$	1.904	1.614	1.557	0.161	3
NIHAO	$\log_{10}(W_{20}/2[\text{km s}^{-1}])$	$\log_{10}(V_{\text{max}}^{\text{DMO}}/[\text{km s}^{-1}])$	1.904	1.751	1.419	0.120	3
NIHAO	$\log_{10}(V_{\text{max}}/[\text{km s}^{-1}])$	$\log_{10}(V_{\text{max}}^{\text{DMO}}/[\text{km s}^{-1}])$	1.904	1.863	1.101	0.032	4
NIHAO	$\log_{10}(V_{\text{HI}}/[\text{km s}^{-1}])$	$\log_{10}(V_{\text{max}}^{\text{DMO}}/[\text{km s}^{-1}])$	1.904	1.833	1.426	0.064	4
NIHAO	$\log_{10}(W_{20}^{\text{max}}/2[\text{km s}^{-1}])$	$\log_{10}(V_{\text{max}}^{\text{DMO}}/[\text{km s}^{-1}])$	1.904	1.855	1.518	0.086	4
NIHAO	$\log_{10}(W_{50}^{\text{max}}/2[\text{km s}^{-1}])$	$\log_{10}(V_{\text{max}}^{\text{DMO}}/[\text{km s}^{-1}])$	1.904	1.742	1.685	0.119	4
NIHAO	$\log_{10}(W_{50}^{\text{med}}/2[\text{km s}^{-1}])$	$\log_{10}(V_{\text{max}}^{\text{DMO}}/[\text{km s}^{-1}])$	1.904	1.640	1.635	0.122	4
SPARC	$\log_{10}(R_1/[\text{kpc}])$	$\log_{10}(M_{\text{star}}/M_{\odot})$	9.493	1.109	0.281	0.18	15
NIHAO	$\log_{10}(R_1/[\text{kpc}])$	$\log_{10}(M_{\text{star}}/M_{\odot})$	8.325	0.779	0.303	0.24	15
SPARC	$\log_{10}(R_{\text{last}}/[\text{kpc}])$	$\log_{10}(M_{\text{star}}/M_{\odot})$	9.471	1.109	0.311	0.23	15
NIHAO	$\log_{10}(R_{90}/[\text{kpc}])$	$\log_{10}(M_{\text{star}}/M_{\odot})$	8.309	0.789	0.252	0.23	15
SPARC	$V \text{ slope}$	$\log_{10}(M_{\text{star}}/M_{\odot})$	9.471	0.123	-0.137	0.19	16
NIHAO	$V \text{ slope}$	$\log_{10}(M_{\text{star}}/M_{\odot})$	8.394	0.286	-0.098	0.14	16
SPARC	$V \text{ slope}$	$\log_{10}(R_{\text{last}}/[\text{kpc}])$	1.109	0.123	-0.399	0.18	16
NIHAO	$V \text{ slope}$	$\log_{10}(R_{90}/[\text{kpc}])$	0.826	0.286	-0.332	0.15	16
NIHAO	$(b/a)_{\text{HI}}$	$\log_{10}(M_{\text{HI}}/M_{\odot})$	8.83	0.585	-0.013	0.20	17

rotation curve shape; non-circular motions, and projection. These are related, but not uniquely, to four ratios, which we show in Fig. 5.

3.1 Inflows and Outflows

The upper left panel shows $V_{\text{max}}/V_{\text{max}}^{\text{DMO}}$, which depends on the net inflow and outflow of baryons. At low velocities the ratio $\simeq 0.85$ indicating net outflows, while at high velocities the ratio is greater than 1, indicating net inflow. As a refer-

ence, if a system lost or did not accrete any of its baryons we would naively expect the ratio of $\sqrt{(1 - f_{\text{bar}})} \simeq 0.92$, where the cosmic baryon fraction, $f_{\text{bar}} = \Omega_{\text{b}}/\Omega_{\text{m}} \simeq 0.15$. However, the reduction in halo velocity is larger than this because the loss of baryons at early times (as a result of the stellar feedback) reduces the accretion rate of dark matter, and hence the halo mass and maximum velocity of the halo by redshift $z = 0$. Similar results are seen in other cosmological hydrodynamical simulations, [Sawala et al. \(e.g., 2016\)](#), so the

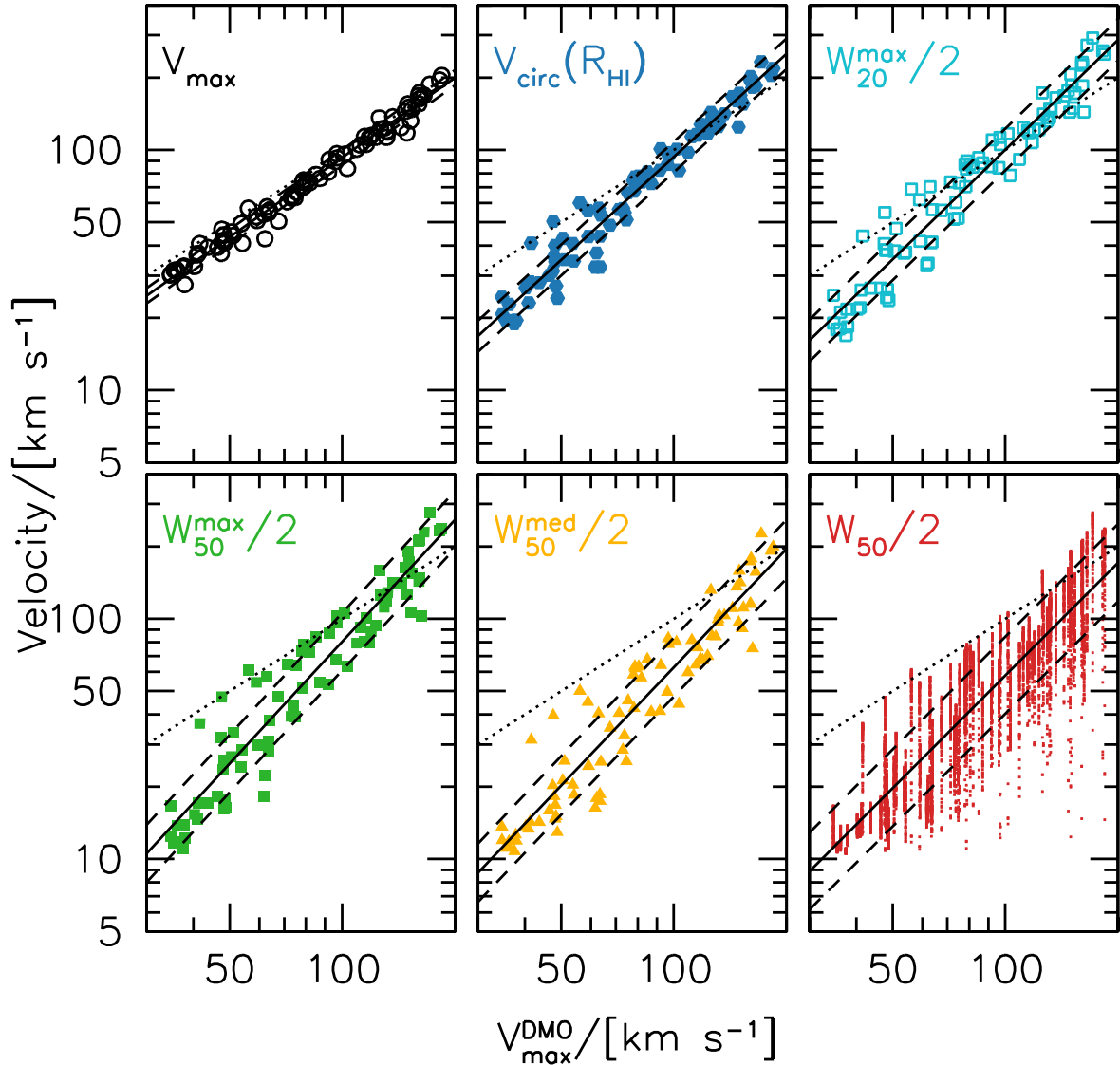


Figure 4. From maximum halo velocity V_{\max}^{DMO} to projected linewidth $W_{50}/2$ for the full sample. Each panel shows a velocity vs V_{\max}^{DMO} relation. A fit to each relation of the form $y = a + b(x - x_0)$ is shown with solid (mean) and dashed (standard deviation) lines. The parameters of the fits are given in Table 1. For reference, the one-to-one line is shown with a dotted line. We see that the slope and scatter get progressively larger as we go from top left to bottom right.

effect appears unrelated to the details of the sub-grid model for star formation and feedback.

3.2 HI extent and rotation curve shape

The upper right panel shows the V_{HI}/V_{\max} ratio vs V_{\max}^{DMO} . In all galaxies V_{HI} is measured at a smaller radius than V_{\max} , so the ratio depends on the shape of the circular velocity profile, and the extent of the HI gas. In high velocity haloes the ratio is greater than 1 because the inflow of baryons. In low mass haloes the ratio is less than 1 because the HI does not extend to the flat part of the velocity profile. At a halo velocity of 50 km/s the average ratio is 0.8, but there are some dwarf galaxies with a ratio of unity and others with a

ratio of 0.6. This is already pointing to diversity of HI extent and/or rotation curve shapes.

3.3 Non-circular motions

The lower left panel shows the $W_{50}^{\text{max}}/2V_{\text{HI}}$ ratio. The linewidth is a convolution of the rotation curve with the HI distribution. In galaxies that are rotationally supported with a flat rotation curve this ratio is close to unity. When the ratio is less than unity this signals a rising rotation curve and/or significant non-circular motions. These can be dispersion in the gas, but also non-axisymmetric features such as bars, spiral arms, and warps, and out of equilibrium gas flows due to e.g., supernova driven winds or mergers. At a

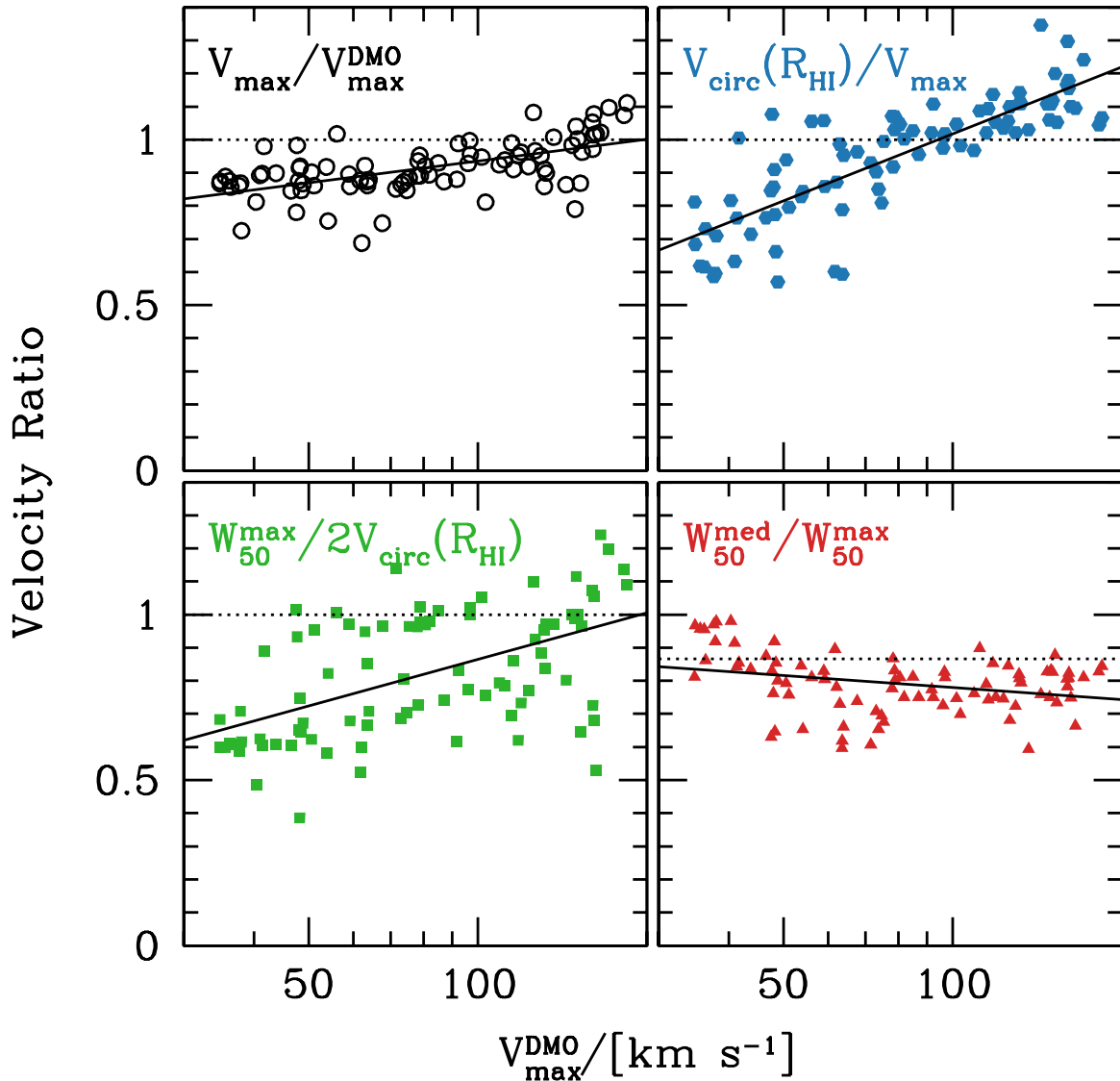


Figure 5. From V_{\max}^{DMO} to projected linewidth W_{50} for the full sample using four independent ratios. Upper left shows $V_{\max}/V_{\max}^{\text{DMO}}$, the ratio between the circular velocities of the hydro and DMO simulation at R_{\max}^{DMO} . This is sensitive to mass in and outflows. The ratio varies from 0.8 to 1.1. Low velocity haloes have ratios less than unity indicating mass loss from the system. Upper right shows V_{HI}/V_{\max} , the ratio between the circular velocity at the HI radius and the circular velocity at R_{\max}^{DMO} . This ratio is sensitive to the shape of the circular velocity profile at the HI radius. The ratio varies from 0.6 to 1.3. High velocity haloes have ratios greater than unity indicating declining velocity profiles, while low mass haloes have ratios less than unity indicating rising velocity profiles. The lower left panel shows $W_{50}^{\max}/2V_{\text{HI}}$, the ratio between the maximum half linewidth and the circular velocity. This is sensitive to non-circular motions and the shape of the rotation curve. This ratio shows the largest variation from 0.4 to 1.2. The lower right panel shows $W_{50}^{\text{med}}/W_{50}^{\max}$, the ratio between the median and maximum linewidths. This ratio is sensitive to the effects of projection and indicates whether galaxies behave like thin rotating disks (dotted line). The ratio varies from 0.6 to 1.0.

halo velocity of 50 km/s the average ratio is 0.7, but again there is significant scatter, with some dwarf galaxies with a ratio close to unity.

3.4 Projection

The lower right panel shows the ratio between the median and maximum W_{50} linewidth. This ratio tells us about projection effects. The inclination angle, i , where $i = 0$ is face-

on, and $i = 90$ is edge-on, is distributed uniformly in $\cos(i)$ from 0 to 1. For a thin rotating disk with negligible velocity dispersion, the linewidth at inclination, i , is related to the linewidth at inclination $i = 90$ by $W_i = \sin(i)W_{90}$. The ratio between the median linewidth ($i = 60$) and the maximum ($i = 90$) is thus $\sin(60) = 0.866$. In the figure we see a few galaxies at all halo velocities near this value (dotted line). However, the majority of galaxies lie below this line indicating the galaxies are in general not thin rotating disks. This is

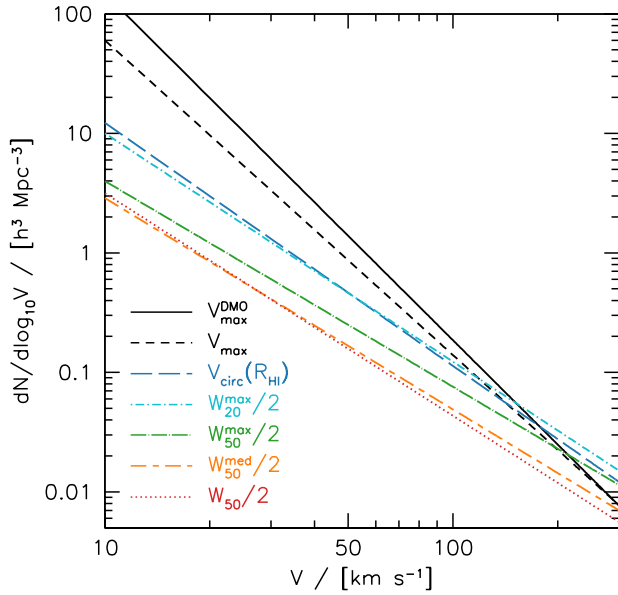


Figure 6. Velocity functions based on different velocity definitions calculated using the fitting formula in Fig.3. The slopes get progressively shallower as we go from maximum dark halo velocity V_{\max}^{DMO} to HI half-linewidth $W_{50}/2$.

another manifestation of the role of non-circular motions. At a halo velocity of 50 km s^{-1} the average ratio is 0.8. At the lowest velocities the ratio is close to unity, indicating these systems (or at least the HI lines) have very little rotational support.

4 IMPLIED VELOCITY FUNCTIONS

We now discuss how the various velocity definitions result in velocity functions with different slopes. First we show results with power-laws, as the transformations are simple and analytic. Then we consider the impact of Gaussian scatter, and finally the actual distribution of linewidths from our simulations corresponding to non-power-laws and non-Gaussian scatter.

4.1 Analytic considerations for the velocity function

For a cumulative velocity function with a power-law form

$$N(> V) = AV^\alpha, \quad (7)$$

the differential velocity function has the same slope, α , but with a normalization that is different by the slope:

$$dN/d \ln V = \alpha N(> V). \quad (8)$$

If two different velocities are related by $V_2 = aV_1^b$, then the cumulative velocity function is simply translated:

$$N(> V_2) = A(V_2/a)^{\alpha/b}. \quad (9)$$

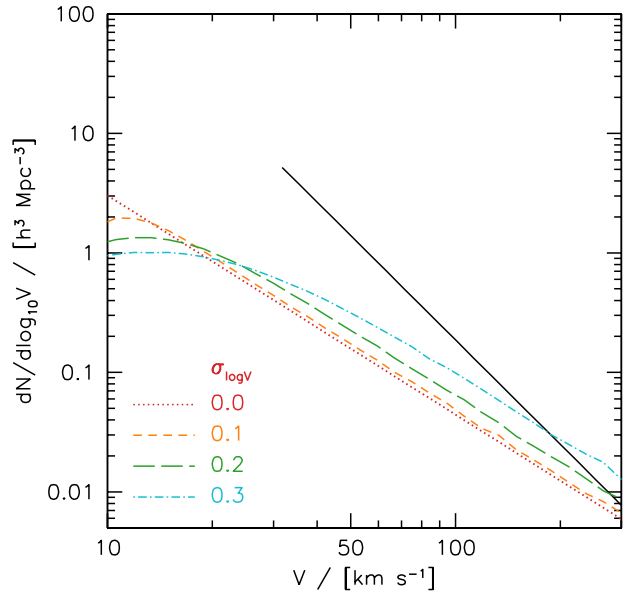


Figure 7. Effect of scatter on the Velocity function. Starting from the $W_{50}/2$ velocity function (red dotted line) we add log-normal scatter of magnitude 0.1 (orange), 0.2 (green), and 0.3 (cyan). Low velocity galaxies get preferentially scattered to high velocities, thereby increasing the normalization of the velocity function. For reference the black line shows the V_{\max}^{DMO} function.

The differential velocity function is changed due to the $d \ln V$, and since

$$d \ln V_1 = (1/b) d \ln V_2, \quad (10)$$

we have the new differential velocity function:

$$dN/d \ln V_2 = (\alpha/b) N(> V_2) = (\alpha/b) A(V_2/a)^{\alpha/b} \quad (11)$$

The differential velocity function for V_{\max}^{DMO} for Cold Dark Matter for a Planck cosmology (Planck Collaboration et al. 2014) is given by (Klypin et al. 2015):

$$dN/d \log_{10} V = 0.186 (V_{\max}^{\text{DMO}}/100)^{-2.9}. \quad (12)$$

We can thus use the equations in Table 1 to translate this into the velocity functions of the various velocity definitions. We first do this ignoring the scatter to show the magnitude of the effect, later we will include the scatter. The result is shown in Fig. 6, and Table 2 gives the slopes and normalizations at $V = 50 \text{ km s}^{-1}$. The majority of the differences come from four conversions: $V_{\max}/V_{\max}^{\text{DMO}} \simeq 0.63$, $V_{\text{HI}}/V_{\max} \simeq 0.53$, $W_{50}^{\text{max}}/2V_{\text{HI}} \simeq 0.54$, and $W_{50}^{\text{med}}/W_{50}^{\text{max}} \simeq 0.67$. The overall shift in normalization is a factor of 8.7. We stress that this is entirely due to a change in the velocities, rather than any change in the number densities of the objects. We note that the strong impact of the velocity definition on the slope of the velocity function has been shown previously by Brook & Shankar (2016) using halo abundance matching to link baryonic masses to halo masses, and then various Baryonic Tully-Fisher relations to relate baryonic masses to velocities.

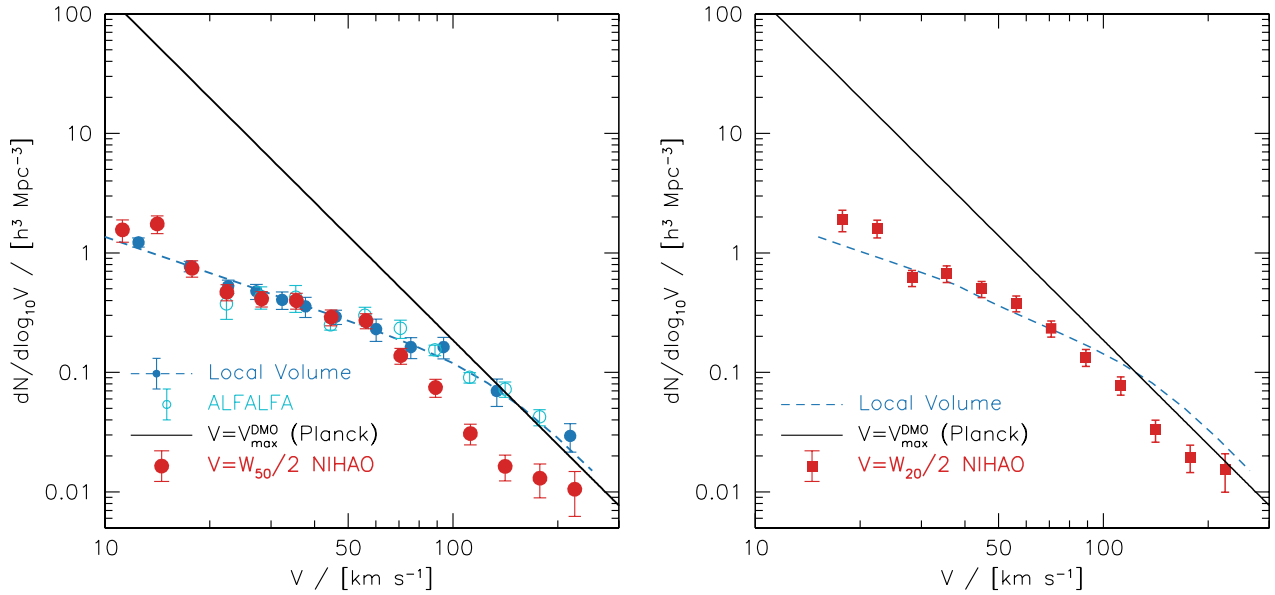


Figure 8. Linewidth velocity function derived from the full distribution of linewidths and V_{\max}^{DMO} in the NIHAO simulations (red points) using $W_{50}/2$ (left) and $W_{20}/2$ (right). The black solid lines show the CDM halo (V_{\max}^{DMO}) velocity function, which has a steep slope of -2.9 . Observational data from the Local Volume and ALFALFA using W_{50} are shown with blue and cyan circles respectively. The blue dashed line shows the fit to the Local Volume from Klypin et al. (2015). In the right panel we transform the observations using the approximation $W_{20} = W_{50} + 25 \text{ km s}^{-1}$, with a minimum $W_{50}/W_{20} = 0.63$.

Table 2. Velocity functions for NIHAO simulations from Fig. 6 of the form $dN/d\log_{10} V = A(V/[50 \text{ km s}^{-1}])^\alpha$.

definition	α	A
V_{\max}^{DMO}	-2.90	1.38
V_{\max}	-2.63	0.867
V_{HI}	-2.03	0.464
$W_{20}^{\text{max}}/2$	-1.91	0.462
$W_{50}^{\text{max}}/2$	-1.72	0.249
$W_{50}^{\text{med}}/2$	-1.77	0.166
$W_{50}/2$	-1.80	0.158

Table 3. Differential velocity functions for NIHAO simulations from Fig. 8.

$\log(V)$	$dN/d\log(V)$ $W_{50}/2$	error	$dN/d\log(V)$ $W_{20}/2$	error
1.05	1.559	0.332	–	–
1.15	1.747	0.295	–	–
1.25	0.743	0.116	1.888	0.385
1.35	0.469	0.072	1.603	0.271
1.45	0.413	0.061	0.617	0.095
1.55	0.398	0.061	0.671	0.107
1.65	0.289	0.044	0.500	0.078
1.75	0.270	0.039	0.378	0.058
1.85	0.138	0.021	0.233	0.036
1.95	0.0747	0.0128	0.134	0.021
2.05	0.0308	0.0060	0.0781	0.0136
2.15	0.0163	0.0040	0.0330	0.0069
2.25	0.0130	0.0041	0.0195	0.0050
2.35	0.0105	0.0043	0.0154	0.0054

4.2 Impact of Gaussian scatter

Fig. 7 shows the impact of Gaussian (in $\log(V)$) scatter on the velocity function. The black line shows the velocity function using V_{\max}^{DMO} , sampled between a velocity of 30 to 200 km s^{-1} . The red dotted line shows the velocity function using $W_{50}/2$. The other lines show the impact of log-normal scatter (0.1, 0.2, and 0.3 dex) in the relation between $W_{50}/2$ and V_{\max}^{DMO} . The effect of scatter is to increase the normalization of the velocity function. Galaxies get preferentially scattered to higher velocity because there are many more low velocity haloes than high velocity haloes. The overall effect is not large, just 0.1 dex change for a scatter of 0.2 dex.

4.3 Deriving the velocity function from linewidth vs maximum circular velocity

We now go into more detail and show how the distribution of galaxies in the $W_{50}/2$ vs V_{\max}^{DMO} plane can be converted into the velocity function. We set up a grid in $x = \log(V_{\max}^{\text{DMO}})$ and $y = \log(W_{50}/2)$ of width dx and dy and count the number of galaxies in each cell, $n(x, y)$. From the cumulative DMO velocity function we straightforwardly know the number of dark matter haloes in a given volume of space, $dN_{\text{CDM}}(x)$. Comparing the actual number of data points $N(x)$ (number of haloes in each x -bin multiplied by

number of projections per halo) to $dN_{\text{CDM}}(x)$ we get the weight $w(x)$ for each halo in bin x :

$$w(x) = \frac{dN_{\text{CDM}}(x)}{N(x)} \quad (13)$$

We then go to each y -bin and count up the number of galaxies using the weights:

$$N(y) = \frac{\sum_x n(x, y) w(x)}{\sum_x w(x)}. \quad (14)$$

As fiducial bin widths we adopt $dx = 0.05$ and $dy = 0.10$. The resulting velocity functions for W_{50} (left) and W_{20} (right) are shown with red points in Fig. 8, and tabulated in Table 3. The error bars (e_y) are calculated as $e_y = y/\sqrt{N}$, where N is the number of simulations that contribute to each y -bin. At low velocities ($W_{50}/2 < 80\text{km s}^{-1}$) the NIHAO $W_{50}/2$ function has a normalization and shallow slope ~ -1 in agreement with observations from the Local Volume (Klypin et al. 2015) and ALFALFA (Papastergis & Shankar 2016). At high velocities ($\gtrsim 100\text{km s}^{-1}$) the NIHAO simulations underpredict the observed number densities, or alternatively the linewidths are too low. We return to a possible cause of this in section 5.3 below.

In our simulations $W_{20}/2$ is a better predictor of the halo velocity than $W_{50}/2$ (See Fig. 4) so this is our preferred definition for future observations. Currently observations of the W_{20} function are not available, so we shift the observations using the approximation $W_{20} = W_{50} + 25\text{km s}^{-1}$ (Brook et al. 2016), and a minimum of $W_{50}/W_{20} = 0.63$. In this case the simulations are closer to the observed velocity function at high velocities, while maintaining the agreement at low velocities.

5 TESTING THE SIMULATIONS

We have shown that the discrepancy at low velocities between the observed HI linewidth function and the $V_{\text{max}}^{\text{DMO}}$ function of LCDM is resolved by the NIHAO simulations. We now discuss in more detail why this is the case, and observational ways in which the simulations can be tested. We focus our discussion on six (mostly dimensionless) parameters that are correlated with the variation in HI linewidth at fixed maximum dark halo velocity.

- Rotation-to-dispersion ratio, $V_{\text{rot}}/\sigma_{\text{HI}}$. The HI dispersion is calculated from the minimum HI linewidth, $\sigma_{\text{HI}} = W_{50}^{\text{min}}/2.35$. For the rotation velocity we use the maximum of the rotation curve, which tends to occur near the HI radius (see Fig. 1 for examples). This definition is not directly observable, but similar definitions are.

- γ_1 , Skewness of the W_{50} distribution, see below for definition. Can be measured on samples of galaxies.

- HI line profile shape, W_{50}/W_{20} . Directly observable.

- Outer circular velocity curve slope, $\Delta \log V/\Delta \log R$. For our simulations is measured between 0.5 and 1.0 R_{HI} . Can be measured for individual galaxies.

- HI-to-virial radius, R_{HI}/R_{200} . Dimensionless, but not directly observable. HI sizes are observable.

- HI disk thickness. Computed as the minimum HI axis ratio from all projections. Can be measured from samples of galaxies.

5.1 Testing rotational support with projection effects

One of the key results from our simulations is that galaxies, and dwarf galaxies in particular, do not always have HI kinematics as expected from idealized thin rotating disks. An observationally testable consequence of this is the effect of projection.

For a thin rotationally supported axisymmetric disk the minor-to-major axis ratio (b/a) is uniformly distributed between 0 and 1. In terms of the disk inclination, i , where $i = 0$ is face-on and $i = 90$ is edge-on, $b/a = \cos(i)$, the observed linewidth then varies as $\sin(i)$. Fig. 9 shows the linewidth vs axis ratio for our four test galaxies. The axis ratio is computed for each projection using moments as described in section 2. The upper galaxies have maximum halo velocity $V_{\text{max}}^{\text{DMO}} \simeq 55\text{km s}^{-1}$, while the lower two galaxies have $V_{\text{max}}^{\text{DMO}} \sim 100\text{km s}^{-1}$. The corresponding stellar masses are $\sim 2 \times 10^8$ and $\sim 10^9 M_{\odot}$, respectively.

The two galaxies on the left panels of Fig. 9 have close to uniform axis ratio distributions (upper histograms) and strongly skewed linewidth distributions (right histograms) close to that predicted for thin disks rotating at the maximum velocity of the dark matter halo (solid red lines). On the other hand, the two galaxies in the right panels of Fig. 9 strongly deviate from this prediction with a lower mean linewidths and a more symmetric distribution of linewidths. The axis ratio distribution is also more centrally concentrated.

A parameter that is related to how rotationally supported a galaxy is, is the skewness of the linewidth distribution. Here we adopt Pearson's moment coefficient of skewness, which is defined as

$$\gamma_1 = \mu_3/\sigma^3. \quad (15)$$

Here $\mu_3 = \Sigma(W - \overline{W})^3/N$ is the third central moment, σ is the standard deviation, and \overline{W} is the mean. A value of $\gamma_1 = 0$ corresponds to a symmetric distribution, $\gamma_1 < 0$ corresponds to a tail to low values, while $\gamma_1 > 0$ corresponds to a tail to high values. A thin rotating disk has a strongly negatively skewed distribution of linewidths with $\gamma_1 = -1.13$.

The galaxies in the left panels of Fig. 9 have $\gamma_1 = -0.97$ and -1.06 , i.e., they behave like thin rotating disks. In contrast the galaxies on the right have $\gamma_1 = -0.10$, and $\gamma_1 = -0.73$, and are thus less rotationally supported systems. These inferences agree with the actual rotation to dispersion ratios ($V_{\text{rot}}/\sigma_{\text{HI}}$).

Another parameter that is related to the rotational support of a galaxy is minimum minor-to-major axis ratio, q_{min} (i.e., the disk thickness). The galaxies on the left have smaller minimum axis ratios (corresponding to thinner edge-on disks): $q_{\text{min}} = 0.11$ and 0.06 compared to 0.28 and 0.25 .

The ratio between linewidths W_{50}/W_{20} , also depends on the rotational support, as well as the circular velocity curve shape, and the extent of the HI. The galaxies on the left have steeper line profiles, and more extended and shallower outer circular velocity curve slopes.

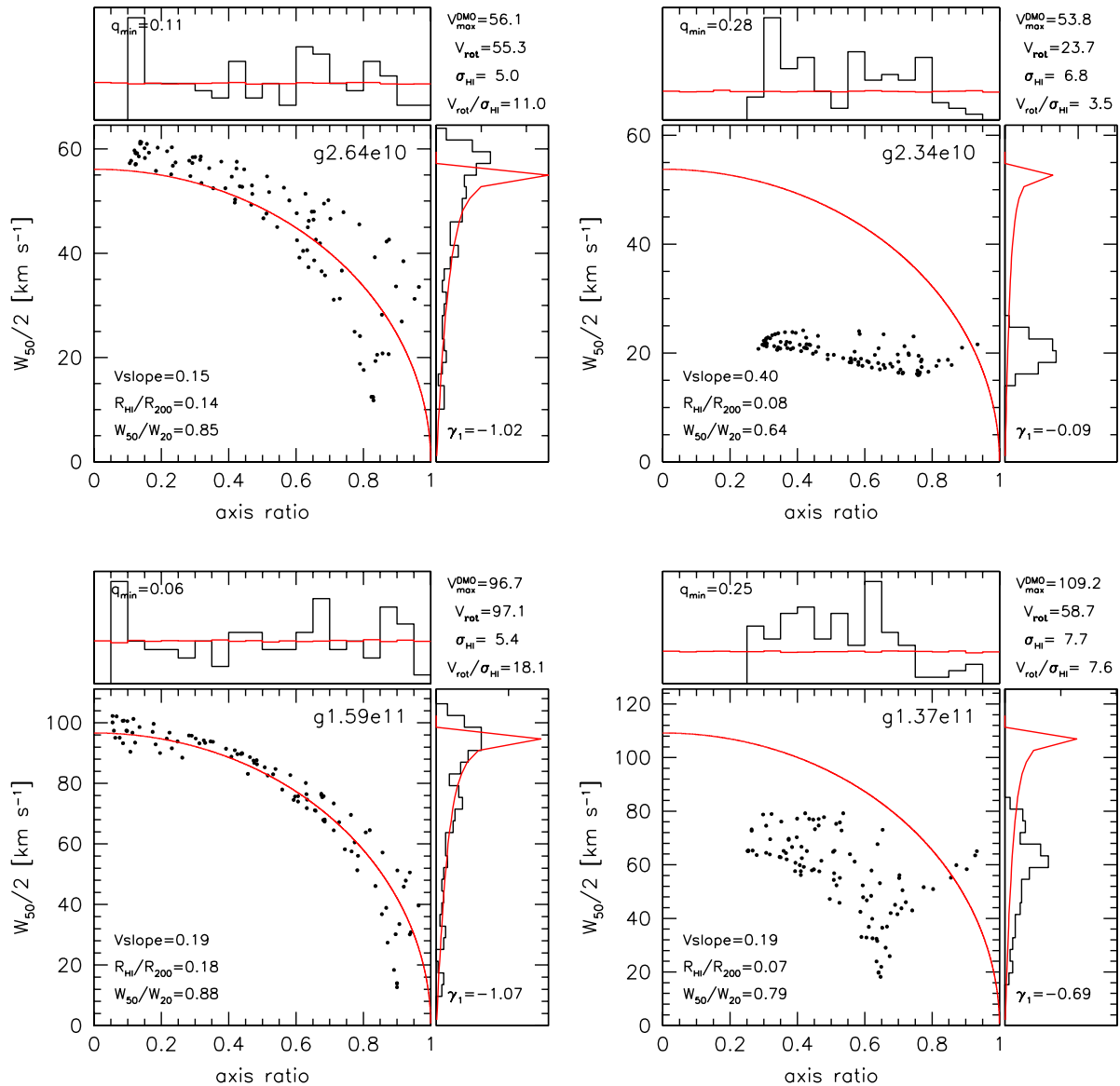


Figure 9. Projection effects in the linewidth vs axis ratio plane for four test galaxies. Upper panels show galaxies with maximum circular velocity $V_{\max}^{\text{DMO}} \sim 55 \text{ km s}^{-1}$, while lower panels show galaxies with $V_{\max}^{\text{DMO}} \sim 100 \text{ km s}^{-1}$. Left panels show rotation dominated galaxies, right panels show galaxies with more pressure support, as can be seen by the thicker HI disks (q_{\min}), and more symmetric distributions of linewidths (γ_1). The red lines show the prediction for a randomly oriented thin disk rotating at (V_{\max}^{DMO}) – uniform axis ratios, and linewidths scaling as $\sin(i)$, where $\cos(i)$ is uniformly distributed.

5.2 What causes linewidths to underestimate maximum circular velocity?

Fig. 10 shows the impact of several (mostly dimensionless) parameters on the relation between median HI linewidth and maximum dark halo circular velocity. The points are color coded by the parameter in question. The four numbers in each panel indicate the mean value of each quartile of points, the solid line is a fit to each quartile of points. We discuss each of them in turn below.

- Outer circular velocity curve slope (top left). A positive value indicates that the curve is still rising in the outer parts, while a value close to zero indicates a flat velocity

curve. Galaxies with more rising circular velocity profiles (red points) tend to have lower linewidth-to-halo velocity ratios.

- HI-to-virial radius (top middle). Smaller galaxies (blue triangles) have lower linewidths. At least partially because if the HI does not reach the flat part of the circular velocity curve, then the kinematics will progressively underestimate the maximum circular velocity.

- HI axis ratio (top right). The thinnest galaxies (red points, $b/a \sim 0.1$) have linewidths that trace the halo velocity, while thicker galaxies have progressively lower linewidths.

- γ_1 , Skewness of the W_{50} distribution (top left). Galaxies

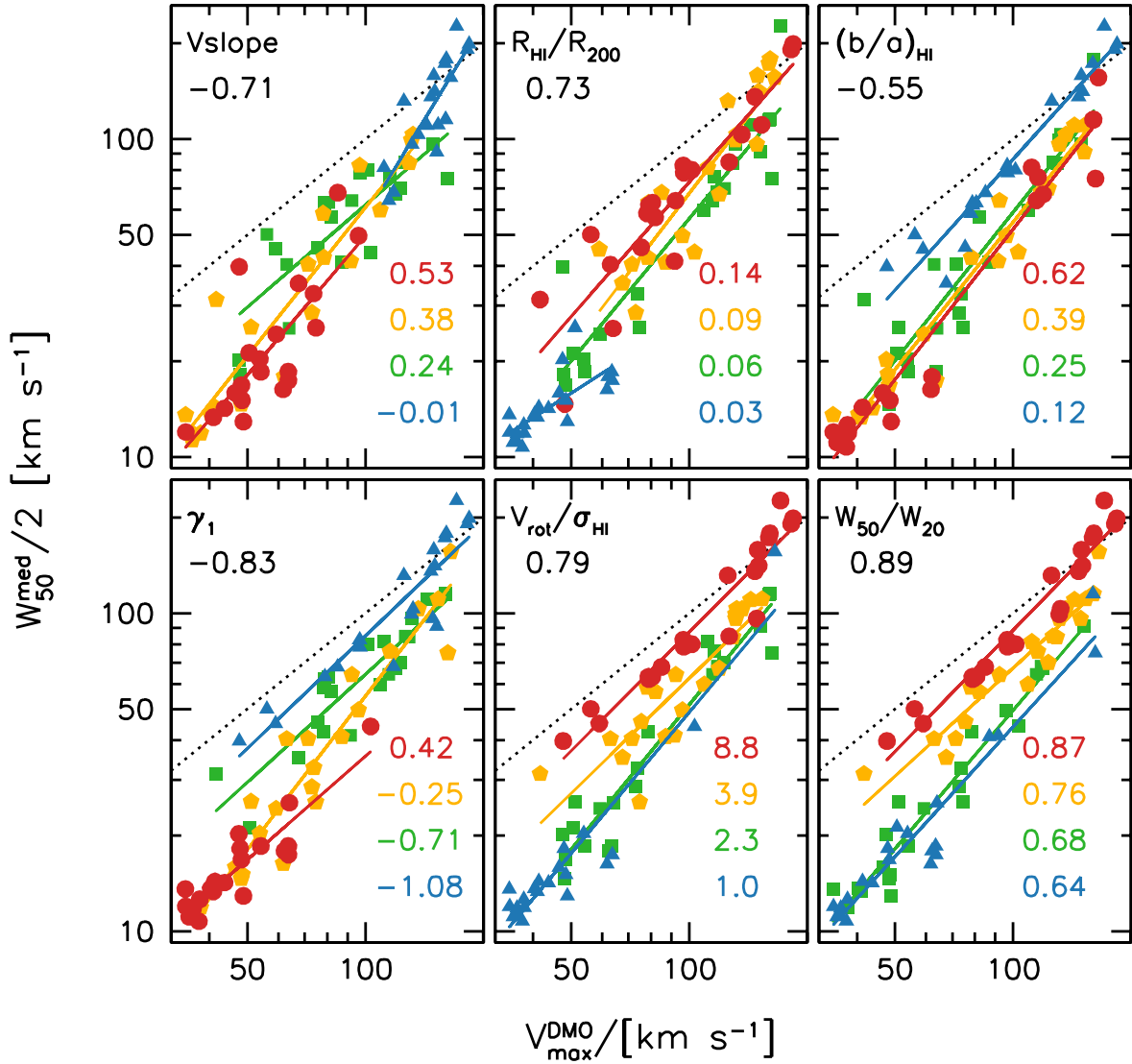


Figure 10. Relation between median HI linewidth and maximum circular velocity of the dark matter halo. Points are color coded by the parameter indicated in the top left corner of each panel. The number at the top left corner is the correlation coefficient between said parameter and $W_{50}^{\text{med}}/2$ and $V_{\text{max}}^{\text{DMO}}$. Structural parameters: logarithmic slope of the outer circular velocity profile (top left); HI-to-virial radius (top middle); minimum minor-to-major HI axis ratio (top right). Kinematic parameters: skewness of the linewidth distribution (bottom left); Rotation-to-dispersion ratio (bottom middle); and linewidth profile shape (bottom right). Each color corresponds to a quartile of the distribution (red are the largest 25%, while blue are the smallest 25%), the mean of each quartile is indicated by the colored numbers.

with strong negative skew (blue points) have linewidths that trace the maximum halo velocity. Larger values of γ_1 result in lower linewidths.

- Rotation-to-dispersion ratio (bottom middle). Rotationally supported systems (red circles) tend to have linewidths that trace the halo velocity, while pressure supported systems (blue triangles) tend to have low linewidths.

- HI line profile shape (bottom left). Steeper line profiles $W_{50}/W_{20} \sim 0.9$ (red points) have linewidths close to halo velocity, while shallow line profiles $W_{50}/W_{20} \sim 0.6$ (blue triangles) have linewidths significantly below the halo velocity.

The profile shape depends on a combination of the rotation curve shape and extent, and the rotation to dispersion ratio.

The number in the top left indicates the correlation coefficient between the specific parameter and $W_{50}^{\text{med}}/2V_{\text{max}}^{\text{DMO}}$. Line profile shape shows the strongest correlation ($\rho = 0.89$) closely followed by the skewness ($\rho = -0.83$), and HI rotation to dispersion ratio ($\rho = 0.79$). At a given halo velocity all six parameter show a correlation with linewidth. To see which of these parameters is most likely to explain the trend with halo mass we show the dependence on halo velocity in Fig. 11. The straight and dashed lines show a fit with 1σ

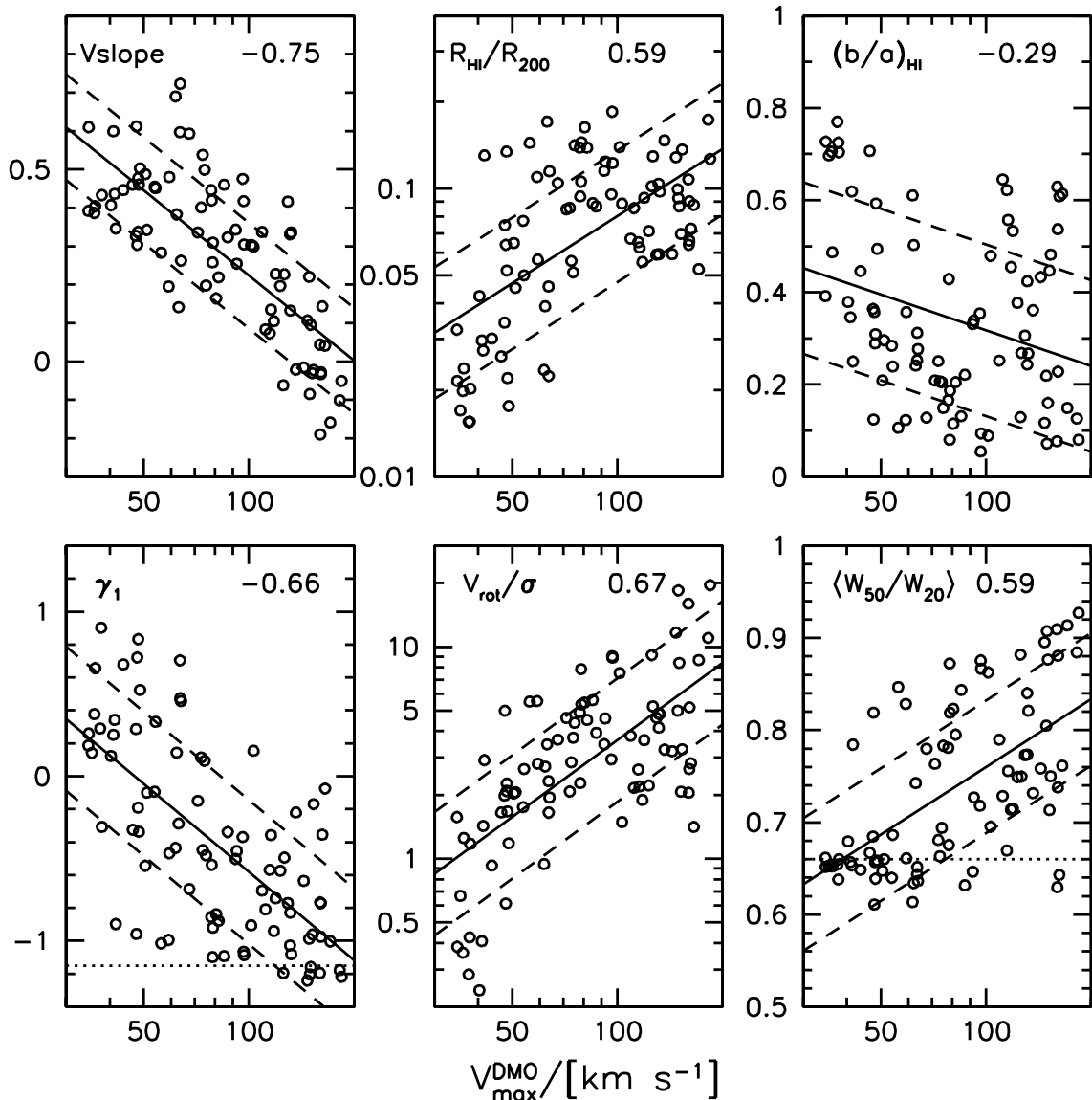


Figure 11. Parameters vs halo velocity. The parameter in question is indicated in the top left corner. The correlation coefficient is given in the top right corner. The mean and standard deviation of a linear fit is shown with solid and dashed lines. Dotted horizontal lines indicate the expectation for a rotating disk (lower left) and Gaussian (lower right).

scatter. The number gives the correlation coefficient. We see clear trends but also significant scatter. Structurally, we see that lower velocity haloes have steeper outer circular velocity curve slopes and relatively smaller HI sizes, and marginally thicker HI disks. Kinematically, we see that lower velocity haloes have less negatively skewed HI linewidth distributions, lower rotation-to-dispersion ratios, and shallower line profiles.

In summary we see that the dependence of W_{50} with V_{\max}^{DMO} is driven primarily by two effects: The degree of rotational support, and the shape of the rotation curve. Galaxies in lower mass halos have less rotational support, and less extended HI. Below we show current observations that show evidence of these two effects.

5.3 Line profile shape

The shape of the HI line profile depends on the amount of rotational support and the shape of the rotation curve. A simple way to parameterize this is the ratio between linewidths measured at the 50% and 20% level of peak flux, W_{50} and W_{20} . The ratio is close to 1 for a rotating disk with a flat rotation curve whose velocity dispersion is small compared to the line-of-sight component of the rotation velocity. As the outer rotation curve slope becomes more positive the ratio decreases, since a larger fraction of the HI flux is coming from gas rotating lower than the maximum. Pressure support also causes ratio to decrease. In the limit $V/\sigma = 0$ the line profile is simply that due to random motions of the gas, and is independent of the rotation curve shape. For a Gaussian $W_{50}/W_{20} = \sqrt{\ln(0.5)/\ln(0.2)} \simeq 0.66$. The

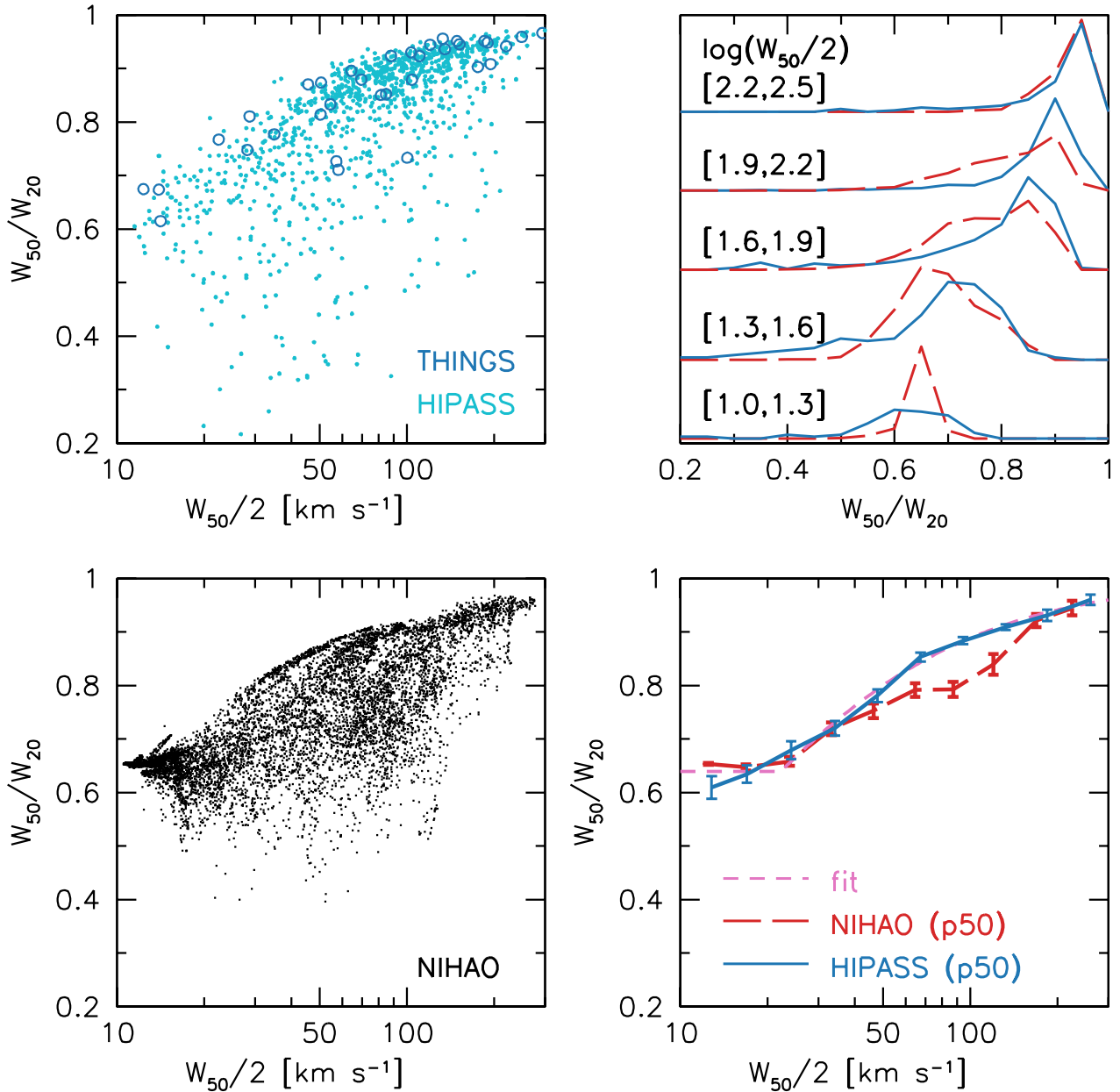


Figure 12. Linewidth ratio W_{50}/W_{20} vs $W_{50}/2$. NIHAO simulations are shown with black points (100 projections per galaxy) and red long-dashed lines. HIPASS observations are shown with cyan points and blue solid lines. THINGS observations are shown with blue circles. The left panels show the distribution of points, the lower right panel shows the median relations, where the error bars show the error on the median. For NIHAO this is the error corresponding to the number of distinct galaxies in each bin, rather than the number of data points (which is ~ 30 times higher). The dashed magenta line is a simple fit to the observations: $W_{20} = W_{50} + 25 \text{ km s}^{-1}$ with a minimum of 0.64. The upper right panel shows the distribution of W_{50}/W_{20} in five bins of $W_{50}/2$ as indicated.

observational advantage of this ratio is it does not require spatially resolved HI observations, which are currently not feasible for large samples of galaxies.

A comparison between NIHAO simulations and observations was previously shown in (Macciò et al. 2016). In both observations and simulations the W_{50}/W_{20} decreases for lower linewidth galaxies. This result was also shown by (Brook et al. 2016) using a smaller sample of galaxies from the MaGICC project (the precursor to NIHAO), and by El-Badry et al. (2018) using galaxies from the FIRE project.

Fig. 12 shows the relation between W_{50} and W_{20} from NIHAO simulations compared to observations from HIPASS (Koribalski et al. 2004) and THINGS (Walter et al. 2008). In both simulations and observations the ratio varies from ~ 0.95 at high velocities to ~ 0.65 at low velocities, and the amount of scatter is also similar. However, when looking at the median relations (lower right panel) the NIHAO simulations underpredict the HIPASS observations for $W_{50} \sim 100 \text{ km s}^{-1}$. This is the same scale where the simulations underpredict the observed velocity function (Fig. 8).

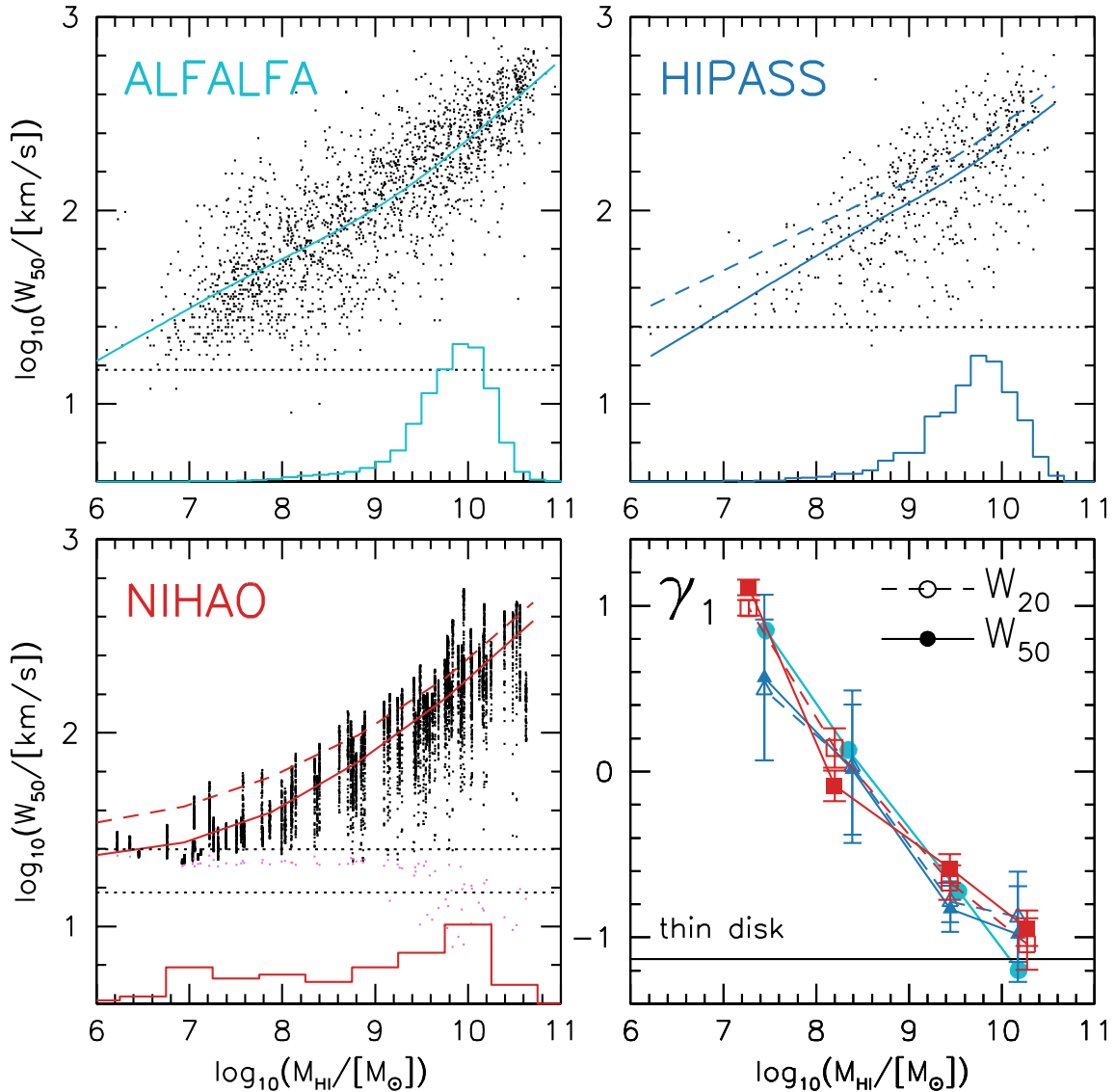


Figure 13. The HI linewidth - mass relation. Upper panels show the observed relations from ALFALFA and HIPASS. Points are W_{50} , solid lines show the mean relation. Dashed lines show the mean relation using W_{20} . Only 100 points per 0.2 dex in mass are plotted to make the change in scatter with mass more apparent. The histogram shows the distribution of mass for the full sample. The horizontal dotted lines show the instrumental velocity resolution limit. The lower left panel shows the relation from NIHAO, where we plot 50 random projections per simulated galaxy. The magenta points show the linewidth due to thermal broadening. The lower right panel shows the skewness of the distribution in bins of mass. Error bars are from bootstrap resampling. An idealized thin rotating disk has $\gamma_1 = -1.13$ (horizontal black line). High mass galaxies in both observations and simulations are close to this value. While lower mass galaxies progressively deviate suggesting more disordered kinematics.

The upper right panel shows the distributions of W_{50}/W_{20} in five bins of $W_{50}/2$. Again this shows an excess of galaxies in NIHAO with low linewidth ratios at intermediate velocities. In principle this could be due to there being too much non-circular motions and/or the HI disks being too small at this velocity scale. Since the NIHAO simulations are in good agreement with observations of HI sizes (see below), we think the low linewidth ratio is more likely due to too an excess of non-circular motions, likely driven by feedback. Due to the large intrinsic variation in W_{50}/W_{20} and the relatively small sample size, another contributing cause could

be sampling effects, i.e., we by chance happen to simulate more galaxies with lower ratios. A similar discrepancy in W_{50}/W_{20} at this velocity scale is seen in the FIRE simulations (El-Badry et al. 2018) and likely has a common origin, which points to feedback driven turbulence.

In summary, the HI line profile shape is a powerful, yet simple test of the simulations, and thus motivates future blind HI surveys obtaining deep enough data to accurately measure both W_{50} and W_{20} .

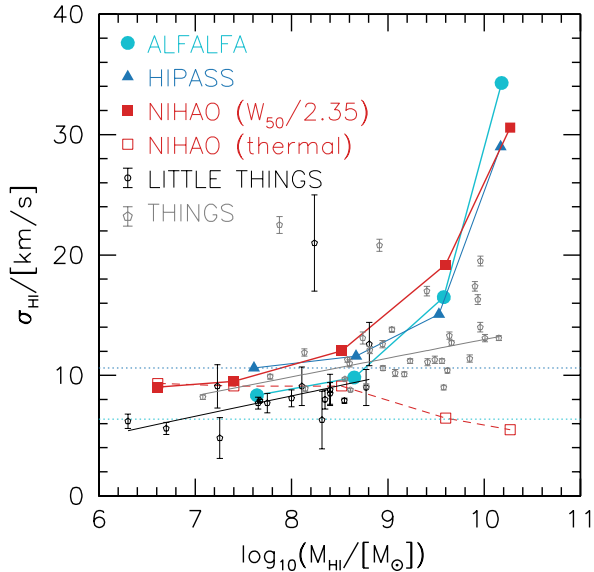


Figure 14. HI velocity dispersion vs HI mass. For NIHAO (red), ALFALFA (cyan), and HIPASS (blue) the velocity dispersion is estimated from the “face-on” linewidths using $\sigma_{\text{HI}} = \langle W_{50} \rangle / 2.35$, where $\langle W_{50} \rangle$ is the average of the lowest 5% of linewidths in a given bin of HI mass. For thin rotating disks, this includes a non-negligible contribution from rotation, so should be considered an upper limit to σ_{HI} . For NIHAO the open squares show the average of the thermal velocity dispersion. The horizontal dotted lines show the resolution limits of ALFALFA (cyan) and HIPASS (blue), and suggest that the HIPASS dispersions are affected by the resolution limit. Measurements for individual galaxies using resolved HI observations from LITTLE THINGS (Iorio et al. 2017) and THINGS (Ianjamasimanana et al. 2012) are shown with black and grey points with error bars, respectively. The lines show fits to these data.

5.4 Skewness of the linewidth distribution

For observed galaxies we only get a single projection per galaxy. However, for a sample of galaxies, we can expect a random distribution of projections, provided we select galaxies by a parameter that is independent of the projection angle, such as the HI mass.

Fig. 13 shows the distributions of HI linewidth vs HI mass. Single dish observations are from the ALFALFA survey (Haynes et al. 2018) and HIPASS (Koribalski et al. 2004). The lower right panel shows the dependence of γ_1 measured in bins of HI mass. The two observational datasets and simulations find consistent results, for the skewness of both W_{50} (solid lines) and W_{20} (dashed lines). Namely high mass galaxies are strongly negatively skewed, close to the value expected for thin rotating disks. Lower mass galaxies have higher γ_1 . This is an observational signature that lower mass galaxies are more kinematically disordered. For the lowest mass galaxies the distribution of linewidths is positively skewed, which is a signature of a floor in the linewidth from thermal broadening of the HI line.

The distribution of linewidths in bins of HI mass can also be used to estimate the velocity dispersion of the HI gas, σ_{HI} . This is because for a galaxy disk that is face-on, there will be zero rotational component projected into the line-of-sight, and thus the observed linewidth will be a reflection of

the disordered motions of the gas. Assuming the line profiles are Gaussian $\sigma_{\text{HI}} = W_{50} / 2.355$. The minimum linewidth is subject to observational measurement errors, and may not be representative of the population, so we take the average of the lowest 5% of linewidths. This will give an upper limit to σ_{HI} because for a thin rotating disk the lowest 5% of inclinations result in a line-of-sight rotation that is $\sim 23\%$ of the edge-on value.

The results of this exercise are shown with the solid points in Fig. 14. Overall there is good agreement between the observations and simulations. In detail there are some differences. Comparing the observations, in the low mass bins HIPASS results in $\sim 3 \text{ km s}^{-1}$ higher σ_{HI} than ALFALFA, likely due to the lower spectral resolution of HIPASS (indicated with horizontal lines). Except for the highest mass bin, the NIHAO simulations have slightly higher σ_{HI} than ALFALFA. For NIHAO the red open squares show the thermal velocity dispersion. The difference between the solid red and open red points is thus the contribution of turbulence (and projected rotation). Since projection affects both simulations and observations the slightly higher dispersions in NIHAO are thus caused by turbulence, likely as a result of the feedback being too strong.

The black and grey points show measurements from individual galaxies using spatially resolved HI observations from THINGS (Ianjamasimanana et al. 2012) and LITTLE THINGS (Iorio et al. 2017). The solid lines show linear fits with 3σ clipping. The slopes are similar, but there is a small offset of $\simeq 2 \text{ km s}^{-1}$, likely reflecting a systematic in the measurement techniques. In the mass range $10^7 < M_{\text{HI}} < 10^9 M_{\odot}$ the resolved measurements are in good agreement with the spatially unresolved linewidth based measurements. Thus in the future our technique can be used to infer the velocity dispersions of large samples of spatially unresolved observations. At higher masses ($M_{\text{HI}} > 10^9 M_{\odot}$) the resolved measurements give lower dispersions than the unresolved measurements. As mentioned above, projected rotation likely contributes to this difference. In addition, the linewidth based dispersion includes deviations from a perfectly axisymmetric disk. For example, a warp will prevent the projected rotation from being zero at any viewing angle, increasing the implied dispersion. Another possible contributing effect is the role of sample selection. The THINGS survey is not a complete sample of galaxies, it is possibly biased towards that more rotation dominated galaxies at these masses than the galaxy population.

In summary, the distribution of linewidths in bins of HI mass shows that in both simulations and observations lower mass galaxies are less rotationally supported than more massive galaxies. This is driven by a reduction in the rotation velocity in low mass galaxies rather than an increase in the gas dispersion, which also decreases in lower mass galaxies.

5.5 HI sizes

We showed previously in Macciò et al. (2016) that the NIHAO galaxies match two HI size vs HI mass relations (the exponential scale length, and the radius where the surface density reaches $1 M_{\odot} \text{ pc}^{-2}$). We are interested in the relation between HI size and halo mass, but halo masses are not directly observable. In the NIHAO simulations, stellar mass is the galaxy observable that is most strongly corre-

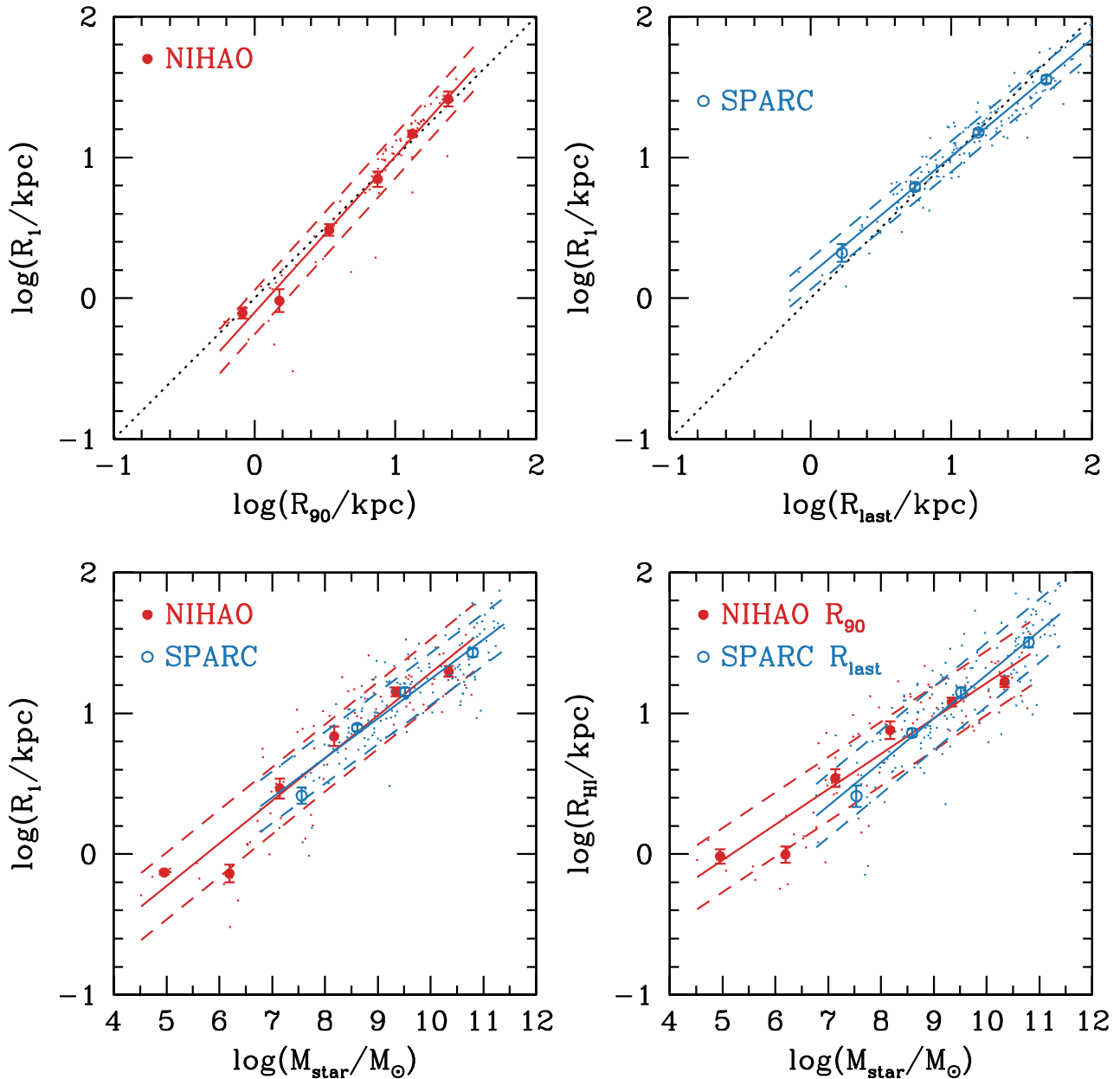


Figure 15. HI size vs stellar mass relation. In the NIHAO simulations (red points) sizes enclose 90% of the HI mass from a face-on projection. In the SPARC observations (blue points) sizes are the last point on the HI rotation curve. Points show individual galaxies, circles show mean sizes in bins of HI mass, the error bar shows the error on the mean, solid and dashed lines show a linear fit and its standard deviation.

lated with halo mass (correlation coefficient of 0.98). The scatter in the stellar mass vs halo mass relation is small (~ 0.2 dex) both in theory (Dutton et al. 2017; Matthee et al. 2017), and observations (More et al. 2011; Reddick et al. 2013; Moster et al. 2018). Here we use galaxies from the SPARC survey (Lelli et al. 2016) as this is the largest compilation of resolved HI rotation curves with $3.6\mu\text{m}$ Spitzer imaging (which gives the most reliable stellar mass tracer).

Fig. 15 shows HI size vs stellar mass relations and a comparison between various HI size definitions. The upper panels show that R_1 (the radius where the HI surface density drops to $1M_{\odot}\text{pc}^{-2}$) is closely related to R_{90} in the NIHAO

simulations and R_{last} in the SPARC observations. The lower left panel shows a very good agreement between the R_1 vs stellar mass relations in NIHAO (red) and SPARC (blue). Fits to the size-mass relations are given in Table 1.

While the observations are not a complete sample of nearby galaxies the comparison is a good place to start. It contradicts the claim by (Trujillo-Gomez et al. 2018) that the HI distribution in NIHAO galaxies is too compact compared to observations. This was suggested by (Trujillo-Gomez et al. 2018) as a reason for the low $W_{50}/2V_{\text{max}}^{\text{DMO}}$ ratio in NIHAO dwarf galaxies. As shown in (Fig. 11), the HI in NIHAO dwarf galaxies is less extended

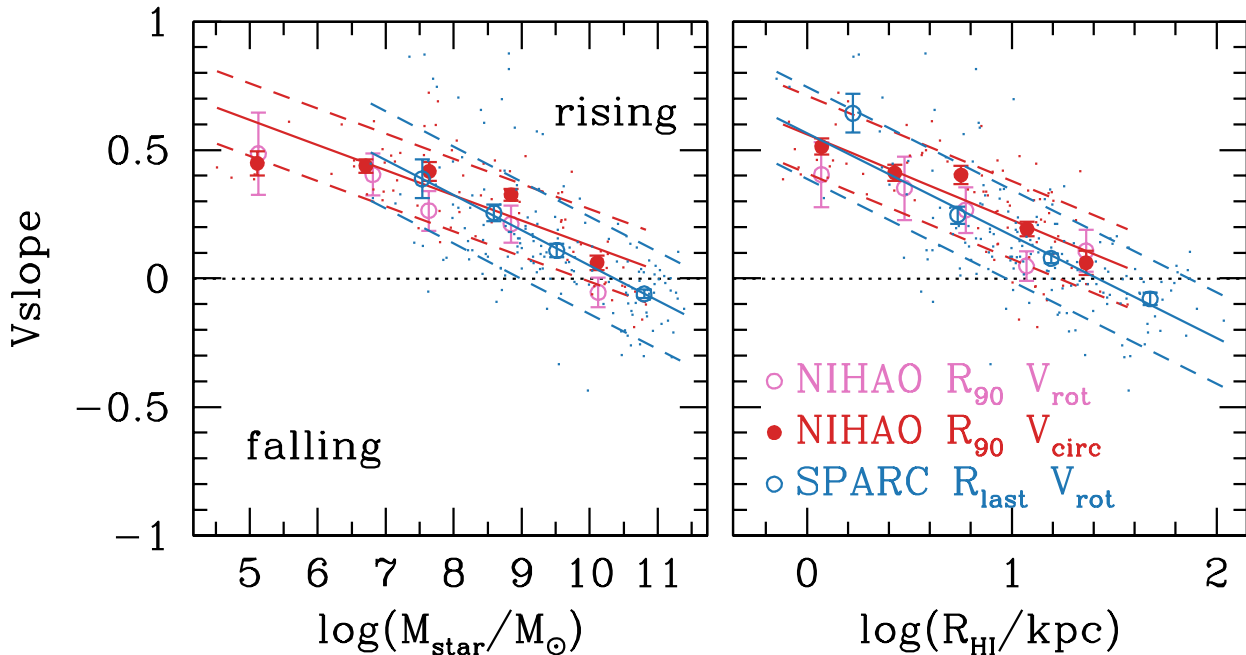


Figure 16. Logarithmic slope of the outer velocity curve vs stellar mass (left) and HI radius (right). In the NIHAO simulations the slope is measured between 0.5 and 1.0 R_{HI} on the circular velocity curve (red) and the rotation velocity curve (pink). For the observations from SPARC (blue) the slope is measured between 0.5 and 1.0 R_{last} on the rotation curve. This shows that in both simulations and observations lower mass and smaller galaxies have more strongly rising velocity curves.

relative to the dark matter halo than in more massive galaxies. So this does contribute to the low $W_{50}/2V_{\text{max}}^{\text{DMO}}$ ratios in dwarfs. However, rather than being an artifact of NIHAO, this appears to be a feature of real galaxies.

5.6 Outer HI rotation curve slopes

Fig. 16 shows the logarithmic slope ($\Delta \log V / \Delta \log R$) of the outer rotation curve vs the stellar mass (left) and the HI radius (right). Points show individual galaxies, while symbols with error bars show the mean and error on the mean in bins of mass or radius. For the observations the slope is measured between 0.5 and 1.0 R_{last} on the rotation curve, for the simulations the fiducial slope is measured between 0.5 and 1.0 R_{HI} on the circular velocity curve (red filled circles), and on the rotation curve (pink open circles).

The simulations are in good agreement with the observations, except that the observed relations have slightly larger scatter, plausibly due to larger measurement errors. We see that high mass or large galaxies have, on average, flat outer rotation curves at the HI radius. As we go to lower stellar masses and smaller sizes the outer rotation curves are progressively rising. Notice that even though both observations and simulations include cored dark matter density profiles in dwarf galaxies, at large radii the typical outer rotation curve slope is ~ 0.5 corresponding to a $\rho \propto r^{-1}$ density profile. When the rotation curve is rising, the half-linewidth $W_{50}/2$ will necessarily underestimate the maximum rotation velocity.

5.7 Axis ratios

Fig. 17 shows the relations between projected axis ratio and HI mass. Each galaxy has 100 projections shown. For clarity we have randomly shifted the HI masses by a small amount for each projection. There is a weak trend, similar to that between minimum axis ratio and halo velocity shown in Fig. 11, with a scatter of 0.20. The average projected axis ratio is about 0.6, compared to 0.5 for an idealized thin disk. The clearest testable prediction is the minimum axis ratio is larger in lower mass galaxies. The most massive galaxies can have disks as thin as 0.05. Below a mass of $M_{\text{HI}} \sim 10^9 M_{\odot}$ the minimum axis ratio steadily increases reaching 0.4 at $M_{\text{HI}} \sim 10^6 M_{\odot}$. The lower envelope (dotted line in Fig. 17) is given by

$$(b/a)_{\text{min}} = 0.06 + 0.106(\log_{10}(M_{\text{HI}}) - 9.4) \quad (16)$$

for $\log_{10}(M_{\text{HI}}) \leq 9.4$, and $(b/a)_{\text{min}} = 0.06$ otherwise.

The cyan circles show observed galaxies from the nearby Universe from Wang et al. (2016). This study combines HI data from several different projects so is representative of a wide variety of galaxy types and environments: Atlas3D (Serra et al. 2012, 2014), Bluedisk (Wang et al. 2013), Faint Irregular Galaxies GMRT Survey (FIGGS) (Begum et al. 2008), LITTLE THINGS (Hunter et al. 2012), Local Volume HI Survey (LVHIS) (Koribalski et al. 2018), starbursting dwarf galaxies (Lelli et al. 2014), The HI Nearby Galaxy Survey (THINGS) (Walter et al. 2008), Ursa Major cluster (Verheijen & Sancisi 2001), Void Galaxy Survey (VGS) (Kreckel et al. 2012), VLA Imaging of Virgo Spirals in Atomic Gas (VIVA) (Chung et al. 2009), Wester-

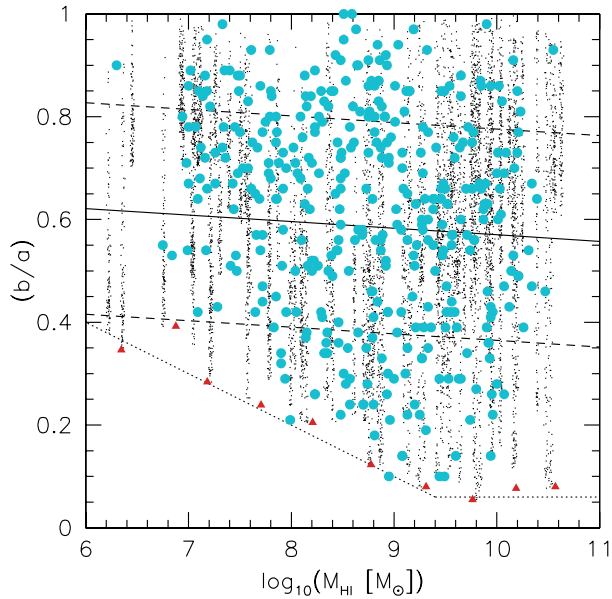


Figure 17. Dependence of projected HI axis ratio on HI mass. For NIHAO simulations each galaxy has 100 projections shown (black points). The red triangles show the minimum axis ratio in bins of mass showing a deficit of small axis ratios in low mass galaxies. This is consistent with observations (cyan circles) from Wang et al. (2016).

work HI survey of spiral and irregular galaxies (WHISP) (Swaters et al. 2002; Noordermeer et al. 2005).

For the vast majority of galaxies (88%) the axis ratio is determined by Wang et al. (2016) from the HI maps, based on the second order moments of the pixel distributions where $\Sigma_{\text{HI}} > 1 M_{\odot} \text{pc}^{-2}$. For the galaxies in VIVA (36) and Atlas3D (8) axis ratios are from tilted ring fits to the velocity fields. Galaxies that are poorly resolved (HI radius less than the beam major axis) have been excluded, though this does not guarantee the axis ratios are well resolved in all galaxies.

The observations and simulations have similar distributions of axis ratios, in particular there are no observed galaxies in the lower left corner where our simulations predict there to be none. This appears to confirm the lack of dwarf galaxies with thin HI disks. Future observations of a complete sample of galaxies with higher spatial resolution are needed to conclusively confirm the lack of thin dwarf galaxies.

6 SUMMARY

We use a sample of 85 galaxies simulated in a LCDM cosmology from the NIHAO project to investigate why HI linewidths systematically underpredict the maximum dark halo circular velocities in dwarf galaxies (Fig. 3). We trace this to two primary effects.

- Lower mass galaxies are less rotationally supported. This is confirmed observationally from the skewness of linewidths in bins of HI mass in both ALFALFA and HIPASS observations (Fig. 13).

- The HI distributions are less extended (relative to the dark matter halo) in dwarf galaxies, so that the rotation curves are still rising at the last measured data point, in agreement with observations (Fig. 16).

The HI profile shape parameterized by W_{50}/W_{20} decreases in lower mass galaxies (Fig. 12) consistent with both these two effects. An additional observational test is in the distribution of HI axis ratios. In particular, in the NIHAO simulations the minimum axis ratio is larger in lower mass galaxies (Fig. 17).

In our simulations the HI kinematics are an inhomogeneous population. There is a significant range of rotational support and HI extent at any given halo or galaxy mass. This variation drives the variation in $W_{50}/2V_{\text{max}}^{\text{DMO}}$ (Fig. 10). Thin and extended rotating HI disks exist in our simulations at all halo masses, but they are not a fair sample. This implies that one cannot use a sample of well ordered rotating disks to interpret the HI linewidths of large unbiased samples of galaxies, as is sometimes done (e.g., Papastergis & Ponomareva 2017; Trujillo-Gomez et al. 2018).

The implied linewidth velocity function from the NIHAO simulations has a shallow slope ($\simeq -1$) at low velocities ($10 < W_{50}/2 < 80 \text{ km s}^{-1}$), consistent with observations (Fig. 8). Thus we conclude that the apparent discrepancy between the predictions of the LCDM cosmological model and observations as highlighted by previous authors (Papastergis et al. 2011; Klypin et al. 2015) is due to their incorrect assumption that $W_{50}/2 \simeq V_{\text{max}}^{\text{DMO}}$.

We look forward to the next generation of blind HI line surveys, APERTIF (Verheijen et al. 2008) and ASKAP (Johnston et al. 2008) that will provide higher spatial resolution data with which to further test our simulations and thus the LCDM model.

ACKNOWLEDGMENTS

We thank the anonymous referee for a detailed and constructive report. This research was carried out on the High Performance Computing resources at New York University Abu Dhabi; on the THEO cluster of the Max-Planck-Institut für Astronomie and on the HYDRA clusters at the Rechenzentrum in Garching. The authors gratefully acknowledge the Gauss Centre for Supercomputing e.V. (www.gauss-centre.eu) for funding this project by providing computing time on the GCS Supercomputer SuperMUC at Leibniz Supercomputing Centre (www.lrz.de). AO is funded by the Deutsche Forschungsgemeinschaft (DFG, German Research Foundation) – MO 2979/1-1.

REFERENCES

- Begum, A., Chengalur, J. N., Karachentsev, I. D., Sharina, M. E., & Kaisin, S. S. 2008, MNRAS, 386, 1667
- Benson, A. J., Frenk, C. S., Lacey, C. G., Baugh, C. M., & Cole, S. 2002, MNRAS, 333, 177
- Binney, J., & Tremaine, S. 1987, Princeton, NJ, Princeton University Press, 1987, 747 p.,
- Brook, C. B., & Di Cintio, A. 2015, MNRAS, 453, 2133
- Brook, C. B., & Shankar, F. 2016, MNRAS, 455, 3841
- Brook, C. B., Santos-Santos, I., & Stinson, G. 2016, MNRAS, 459, 638

- Brooks, A. M., Papastergis, E., Christensen, C. R., et al. 2017, *ApJ*, 850, 97
- Buck, T., Macciò, A. V., Dutton, A. A., Obreja, A., & Frings, J. 2018, *MNRAS* in press, arXiv:1804.04667
- Bullock, J. S., Kravtsov, A. V., & Weinberg, D. H. 2000, *ApJ*, 539, 517
- Courteau, S. 1997, *AJ*, 114, 2402
- Chung, A., van Gorkom, J. H., Kenney, J. D. P., Crawl, H., & Vollmer, B. 2009, *AJ*, 138, 1741
- Ceverino, D., Primack, J., Dekel, A., & Kassín, S. A. 2017, *MNRAS*, 467, 2664
- Dutton, A. A., & Macciò, A. V. 2014, *MNRAS*, 441, 3359
- Dutton, A. A., Obreja, A., Wang, L., et al. 2017, *MNRAS*, 467, 4937
- El-Badry, K., Quataert, E., Wetzel, A., et al. 2018a, *MNRAS*, 473, 1930
- El-Badry, K., Bradford, J., Quataert, E., et al. 2018b, *MNRAS*, 477, 1536
- Gill, S. P. D., Knebe, A., & Gibson, B. K. 2004, *MNRAS*, 351, 399
- Gutcke, T. A., Stinson, G. S., Macciò, A. V., Wang, L., & Dutton, A. A. 2017, *MNRAS*, 464, 2796
- Haynes, M. P., Giovanelli, R., Kent, B. R., et al. 2018, *ApJ*, 861, 49
- Hunter, D. A., Ficut-Vicas, D., Ashley, T., et al. 2012, *AJ*, 144, 134
- Ianjamasimanana, R., de Blok, W. J. G., Walter, F., & Heald, G. H. 2012, *AJ*, 144, 96
- Iorio, G., Fraternali, F., Nipoti, C., et al. 2017, *MNRAS*, 466, 4159
- Jarosik, N., Bennett, C. L., Dunkley, J., et al. 2011, *ApJS*, 192, 14
- Johnston, S., Taylor, R., Bailes, M., et al. 2008, *Experimental Astronomy*, 22, 151
- Kassin, S. A., Weiner, B. J., Faber, S. M., et al. 2012, *ApJ*, 758, 106
- Knollmann, S. R., & Knebe, A. 2009, *ApJS*, 182, 608
- Koribalski, B. S., Staveley-Smith, L., Kilborn, V. A., et al. 2004, *AJ*, 128, 16
- Koribalski, B. S., Wang, J., Kamphuis, P., et al. 2018, *MNRAS*, Klypin, A., Kravtsov, A. V., Valenzuela, O., & Prada, F. 1999, *ApJ*, 522, 82
- Klypin, A., Karachentsev, I., Makarov, D., & Nasonova, O. 2015, *MNRAS*, 454, 1798
- Kravtsov, A. V., Gnedin, O. Y., & Klypin, A. A. 2004, *ApJ*, 609, 482
- Kravtsov, A. V. 2013, *ApJ*, 764, L31
- Kreckel, K., Platen, E., Aragón-Calvo, M. A., et al. 2012, *AJ*, 144, 16
- Lelli, F., Verheijen, M., & Fraternali, F. 2014, *A&A*, 566, A71
- Lelli, F., McGaugh, S. S., & Schombert, J. M. 2016, *AJ*, 152, 157
- Macciò, A. V., Kang, X., Fontanot, F., et al. 2010, *MNRAS*, 402, 1995
- Macciò, A. V., Udrescu, S. M., Dutton, A. A., et al. 2016, *MNRAS*, 463, L69
- Matthee, J., Schaye, J., Crain, R. A., et al. 2017, *MNRAS*, 465, 2381
- Moore, B., Ghigna, S., Governato, F., et al. 1999, *ApJ*, 524, L19
- More, S., van den Bosch, F. C., Cacciato, M., et al. 2011, *MNRAS*, 410, 210
- Moster, B. P., Naab, T., & White, S. D. M. 2018, *MNRAS*, 477, 1822
- Newman, S. F., Genzel, R., Förster Schreiber, N. M., et al. 2013, *ApJ*, 767, 104
- Noordermeer, E., van der Hulst, J. M., Sancisi, R., Swaters, R. A., & van Albada, T. S. 2005, *A&A*, 442, 137
- Obreschkow, D., Ma, X., Meyer, M., et al. 2013, *ApJ*, 766, 137
- Papastergis, E., Martin, A. M., Giovanelli, R., & Haynes, M. P. 2011, *ApJ*, 739, 38
- Papastergis, E., & Shankar, F. 2016, *A&A*, 591, A58
- Papastergis, E., & Ponomareva, A. A. 2017, *A&A*, 601, A1
- Planck Collaboration, Ade, P. A. R., Aghanim, N., et al. 2014, *A&A*, 571, A16
- Rahmati, A., Schaye, J., Pawlik, A. H., & Raičević, M. 2013, *MNRAS*, 431, 2261
- Reddick, R. M., Wechsler, R. H., Tinker, J. L., & Behroozi, P. S. 2013, *ApJ*, 771, 30
- Santos-Santos, I. M., Di Cintio, A., Brook, C. B., et al. 2018, *MNRAS*, 473, 4392
- Sawala, T., Frenk, C. S., Fattahi, A., et al. 2016, *MNRAS*, 457, 1931
- Schneider, A., Anderhalden, D., Macciò, A. V., & Diemand, J. 2014, *MNRAS*, 441, L6
- Schneider, A., & Trujillo-Gomez, S. 2018, *MNRAS*, 475, 4809
- Serra, P., Oosterloo, T., Morganti, R., et al. 2012, *MNRAS*, 422, 1835
- Serra, P., Oser, L., Krajnović, D., et al. 2014, *MNRAS*, 444, 3388
- Springel, V., White, S. D. M., Jenkins, A., et al. 2005, *Nature*, 435, 629
- Stinson, G., Seth, A., Katz, N., et al. 2006, *MNRAS*, 373, 1074
- Stinson, G. S., Brook, C., Macciò, A. V., et al. 2013, *MNRAS*, 428, 129
- Stinson, G. S., Dutton, A. A., Wang, L., et al. 2015, *MNRAS*, 454, 1105
- Swaters, R. A., van Albada, T. S., van der Hulst, J. M., & Sancisi, R. 2002, *A&A*, 390, 829
- Trujillo-Gomez, S., Klypin, A., Primack, J., & Romanowsky, A. J. 2011, *ApJ*, 742, 16
- Trujillo-Gomez, S., Schneider, A., Papastergis, E., Reed, D. S., & Lake, G. 2018, *MNRAS*, 475, 4825
- Verbeke, R., Papastergis, E., Ponomareva, A. A., Rath, S., & De Rijcke, S. 2017, *A&A*, 607, A13
- Verheijen, M. A. W., & Sancisi, R. 2001, *A&A*, 370, 765
- Verheijen, M. A. W., Oosterloo, T. A., van Cappellen, W. A., et al. 2008, *The Evolution of Galaxies Through the Neutral Hydrogen Window*, 1035, 265
- Walter, F., Brinks, E., de Blok, W. J. G., et al. 2008, *AJ*, 136, 2563
- Wang, J., Kauffmann, G., Józsa, G. I. G., et al. 2013, *MNRAS*, 433, 270
- Wang, L., Dutton, A. A., Stinson, G. S., et al. 2015, *MNRAS*, 454, 83
- Wang, J., Koribalski, B. S., Serra, P., et al. 2016, *MNRAS*, 460, 2143
- Wadsley, J. W., Keller, B. W., & Quinn, T. R. 2017, *MNRAS*, 471, 2357
- Wisnioski, E., Förster Schreiber, N. M., Wuyts, S., et al. 2015, *ApJ*, 799, 209
- Zavala, J., Jing, Y. P., Faltenbacher, A., et al. 2009, *ApJ*, 700, 1779
- Zwaan, M. A., Meyer, M. J., & Staveley-Smith, L. 2010, *MNRAS*, 403, 1969